Representation of the Subgrid-Scale Turbulent Transport in Convective Boundary Layers at Gray-Zone Resolutions

HYEYUM HAILEY SHIN

National Center for Atmospheric Research, Boulder, Colorado*

SONG-YOU HONG

Korea Institute of Atmospheric Prediction Systems, Seoul, South Korea

(Manuscript received 6 April 2014, in final form 1 September 2014)

ABSTRACT

Parameterization of the unresolved vertical transport in the planetary boundary layer (PBL) is one of the key physics algorithms in atmospheric models. This study attempts to represent the subgrid-scale (SGS) turbulent transport in convective boundary layers (CBLs) at gray-zone resolutions by investigating the effects of grid-size dependency in the vertical heat transport parameterization for CBL simulations. The SGS transport profile is parameterized based on the 2013 conceptual derivation by Shin and Hong. First, nonlocal transport via strong updrafts and local transport via the remaining small-scale eddies are separately calculated. Second, the SGS nonlocal transport is formulated by multiplying a grid-size dependency function with the total nonlocal transport profile fit to the large-eddy simulation (LES) output. Finally, the SGS local transport is formulated by multiplying a grid-size dependency function with the total local transport profile, which is calculated using an eddy-diffusivity formula. The new algorithm is evaluated against the LES output and compared with a conventional nonlocal PBL parameterization.

For ideal CBL cases, by considering the scale dependency in the parameterized vertical heat transport, improvements over the conventional nonlocal *K*-profile model appear in mean profiles, resolved and SGS vertical transport profiles with their grid-size dependency, and the energy spectrum. Real-case simulations for convective rolls show that the simulated roll structures are more robust with stronger intensity when the new algorithm is used.

1. Introduction

Hopes for kilometer- or sub-kilometer-scale numerical simulations have been realized in recent decades thanks to increase in computing power. Many operational numerical weather prediction (NWP) centers are now running their models using 2–10-km horizontal resolution (Davies et al. 2005; Saito et al. 2006; Charles and Colle 2009; Baldauf et al. 2011; Seity et al. 2011), and some will be reaching sub-kilometer grid size within a few years (Hong and Dudhia 2012). Several research communities have run kilometer-scale cloud-resolving models (CRMs) since the late 1980s (e.g., Weisman et al. 1988), and recently, a 100-m-resolution large-eddy simulation (LES) with a domain of 205 km × 205 km × 27 km was conducted for cloud systems (Khairoutdinov et al. 2009).

A number of previous studies have reported the advantages of kilometer-scale high-resolution modeling against coarser-resolution modeling, in qualitative and quantitative views (Weisman et al. 2008; Davis et al. 2008; Clark et al. 2009; Langhans et al. 2013). Moreover, the resolution at 1–4 km has been deemed as cloud-resolving scale because this grid mesh size is comparable to or smaller than the cloud diameter and cumulus parameterization schemes (CPSs) can be turned off "in the view of cloud microphysics" (i.e., the cloud fraction of a grid is either 0 or 1 at this resolution) (Arakawa et al. 2011). However, limitations and uncertainties still persist regarding the physics processes occurring at subgrid

---

* The National Center for Atmospheric Research is sponsored by the National Science Foundation.

Corresponding author address: Hyeyum Hailey Shin, National Center for Atmospheric Research, P.O. Box 3000, Boulder, CO 80307-3000.
E-mail: hshin@ucar.edu

DOI: 10.1175/MWR-D-14-00116.1

scales (Bryan et al. 2003; Moeng et al. 2010; Bryan and Morrison 2012; Moeng and Arakawa 2012). The kilometer-resolution CRMs can resolve the bulk characteristics of convective cloud systems, but a grid spacing of $O(100)$ m is needed to resolve an inertial subrange of the systems "in the view of turbulence" and to appropriately use the LES subgrid-scale (SGS) turbulence model for their design (Bryan et al. 2003). That is, the gray-zone problem of the SGS turbulence models arises.

The gray zone for the SGS turbulence models is also called "terra incognita" by the pioneering study addressing this issue (Wyngaard 2004). In brief, in terra incognita, the energy-containing turbulence scale (l) and the scale of the spatial filter (Δ) are comparable, and none of the traditional turbulence modeling methods was designed for this resolution [i.e., LES ($\Delta \ll l$) or mesoscale modeling using one-dimensional parameterizations ($\Delta \gg l$)]. In deep moist convection and convective boundary layers (CBLs), l has a size of order of a kilometer, indicating that errors related to assumptions in the parameterizations are expected in the near-kilometer resolution simulations (e.g., Bryan et al. 2003; LeMone et al. 2010, hereafter L10; Moeng et al. 2010; Fiori et al. 2010; Honnert et al. 2011; Ching et al. 2014). In the present study, we focus on the gray-zone problem in CBLs at an intermediate scale between LES and PBL parameterization.

The gray-zone problem causes conflicting simulation results, according to the magnitude and/or contribution of a nonlocal transport term in the SGS turbulence model used. Here, the nonlocal transport is defined as the vertical transport via strong updrafts of coherent structures (e.g., thermals, rolls, and cells) (Siebesma and Cuijpers 1995; Siebesma et al. 2007). When the PBL parameterizations including the nonlocal transport term (i.e., nonlocal PBL parameterizations) are used in the gray zone and the nonlocal term is large to such a degree that the coherent structures are considered as completely SGS, the SGS turbulent transport is excessively estimated such that resolved motions are weakened (e.g., Honnert et al. 2011; LeMone et al. 2013; Ching et al. 2014). The conventional nonlocal PBL parameterizations express the nonlocal transport through a mass-flux term (e.g., Pleim 2007; Siebesma et al. 2007; Pergaud et al. 2009) or a gradient-adjustment gamma term (e.g., Troen and Mahrt 1986; Holtslag and Boville 1993; Hong et al. 2006). On the other hand, the local SGS models bring the opposite results. The local SGS models include the LES-type SGS models [e.g., Deardorff-type turbulent kinetic energy (TKE) model] and local PBL schemes (e.g., Mellor–Yamada-type TKE scheme). When only local models are used without the nonlocal term, the SGS vertical transport tends to be underestimated, resulting in overestimation of the resolved part (Takemi and Rotunno 2003; Cheng et al. 2010; Honnert et al. 2011; LeMone et al. 2013). Therefore, through a practical point of view, how to accurately estimate the nonlocal SGS transport in the gray zone while leaving a correct amount of energy for the resolved motion is a prime question for solving the gray-zone problem.

Recently, Shin and Hong (2013, hereafter SH13) computed the grid-size dependencies of SGS nonlocal and local vertical transports in CBLs at gray-zone resolutions, using a 25-m-resolution LES as the benchmark. They produced reference data for gray-zone grid spacing by spatially filtering the benchmark LES. The reference data at each grid size (Δ) show the amount of SGS vertical transport that has to be parameterized at Δ. SH13 showed that the nonlocal part determines the scale dependency of the total (nonlocal plus local) SGS transport. This is consistent with the key finding of Honnert et al. (2011), who revealed that the inclusion of the mass-flux term is more important than the formulation of eddy diffusivity in determining the grid-size dependency of the parameterized transport in the gray zone.

Figure 1 presents the vertical profiles of the domain-averaged SGS nonlocal and local heat transports derived from the reference data for a CBL forced by strong surface heat flux ($\overline{w'\theta'}_{\mathrm{SFC}} = 0.20\,\mathrm{K\,m\,s^{-1}}$) and moderate geostrophic wind ($U_g = 10.0\,\mathrm{m\,s^{-1}}$). A brief description of the reference data is included in the appendix. The magnitude of the SGS nonlocal transport is larger than that of its local counterpart throughout most of the CBL. The strong updrafts (i.e., the nonlocal transport) play a role in cooling the surface layer and heating the mixed layer, and they produce negative heat flux in the entrainment zone (Fig. 1a). This finding is consistent with that of Hellsten and Zilitinkevich (2013), who used time-averaging filtering and Fourier filtering to separate the convective organized structures and background turbulence. The remaining background turbulence operates in opposite directions to the strong updrafts in the surface layer and entrainment zone (Fig. 1b). The magnitudes of the SGS nonlocal and local transport terms decrease according to grid size at different rates, but the role of each term is maintained with varying grid size.

In this study, we investigate the effects of scale dependency in parameterized vertical transport on CBL simulations at gray-zone resolutions by suppressing the role of SGS parameterization using explicit grid-size dependency functions derived by SH13. Note that the study of SH13 was limited to formulating the grid-size functions and determining factors that affect the functions. Here, we extend the work to the application of the formula to CBL simulations by designing a vertical

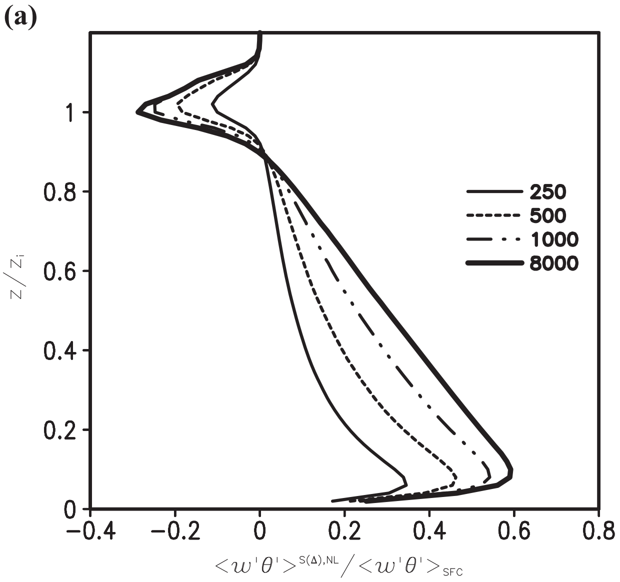

FIG. 1. Vertical profiles of the domain-averaged (a) SGS nonlocal and (b) SGS local heat transports for Δ = 250 m (thin solid), 500 m (thin dotted), 1000 m (thin dot–dot–dashed), and 8000 m (thick solid), normalized by surface heat flux.

transport algorithm and evaluating its performance in a three-dimensional model framework. Recently, there have been several studies that modified existing PBL parameterizations for improving their performance in the gray zone [Boutle et al. (2014) for a K-profile model; Honnert et al. (2014) for a mass-flux scheme; Ito et al. (2014) for the Mellor–Yamada scheme]. To the author's knowledge, however, there is no literature that both evaluated the gray-zone PBL parameterization against LES results and applied it to real-case simulations.

The rest of this paper is organized as follows. Section 2 describes the algorithm for reducing the SGS vertical transport according to grid size. Its effects are evaluated for idealized CBL simulations and real-case convective roll simulations in section 3. Summary and conclusions follow in the final section.

2. An algorithm for resolution-dependent SGS transport

To reduce the SGS heat transport according to grid size (Fig. 1), we design a new SGS model based on SH13. The nonlocal and local fluxes are separately parameterized as in the conventional nonlocal PBL schemes because they have different scale dependencies.

a. Nonlocal heat transport

To parameterize the subgrid-scale nonlocal heat transport at resolution Δ, the total nonlocal transport profile ($\langle w'\theta'\rangle^{\mathrm{NL}}$; hereafter, the angle brackets refer to a domain average) is modeled and then multiplied by $P_{\mathrm{NL}}(\Delta_{*\mathrm{cs}})$ [$\Delta_{*\mathrm{cs}} \equiv \Delta/(C_{\mathrm{cs}} z_i) = \Delta_*/C_{\mathrm{cs}}$, where $\Delta_* \equiv \Delta/z_i$; z_i is the PBL height and C_{cs} is a stability function]:

$$\langle w'\theta'\rangle^{S(\Delta_*),\mathrm{NL}} = \langle w'\theta'\rangle^{\mathrm{NL}} P_{\mathrm{NL}}(\Delta_{*\mathrm{cs}}), \tag{1}$$

$$P_{\mathrm{NL}}(\Delta_{*\mathrm{cs}}) = 0.243\frac{(\Delta_{*\mathrm{cs}})^2 + 0.936(\Delta_{*\mathrm{cs}})^{7/8} - 1.110}{(\Delta_{*\mathrm{cs}})^2 + 0.312(\Delta_{*\mathrm{cs}})^{7/8} + 0.329} + 0.757, \tag{2}$$

$$C_{\mathrm{cs}} = a_{\mathrm{cs}}[\tanh(b_{\mathrm{cs}}|u_*/w_* + c_{\mathrm{cs}}| + d_{\mathrm{cs}}) + e_{\mathrm{cs}}]. \tag{3}$$

In Eq. (1), the superscripts S and NL designate SGS and nonlocal, respectively. The term $P_{\mathrm{NL}}(\Delta_{*\mathrm{cs}})$ (Fig. 2a; for $C_{\mathrm{cs}} = 1$) is the grid-size dependency function of the SGS nonlocal heat transport suggested by SH13, and an empirical function fit into the reference data for a free-convection case.

SH13 showed that the gray-zone grid size, where the resolved and SGS partitions are equal, increases as u_*/w_* increases for u_*/w_* in a certain limit: u_* is the surface friction velocity and w_* is the convective velocity scale. This is because the coherent large-eddy structures change from thermal circulations ($\sim 1.5z_i$) to horizontal rolls ($\sim 3z_i$), and the energy spectral peak moves to a larger scale. The quantity C_{cs} is a stability function defined for applying this effect to the grid-size dependency (Fig. 2b). The coefficients a_{cs}–e_{cs} in Eq. (3) are determined to satisfy the conditions below:

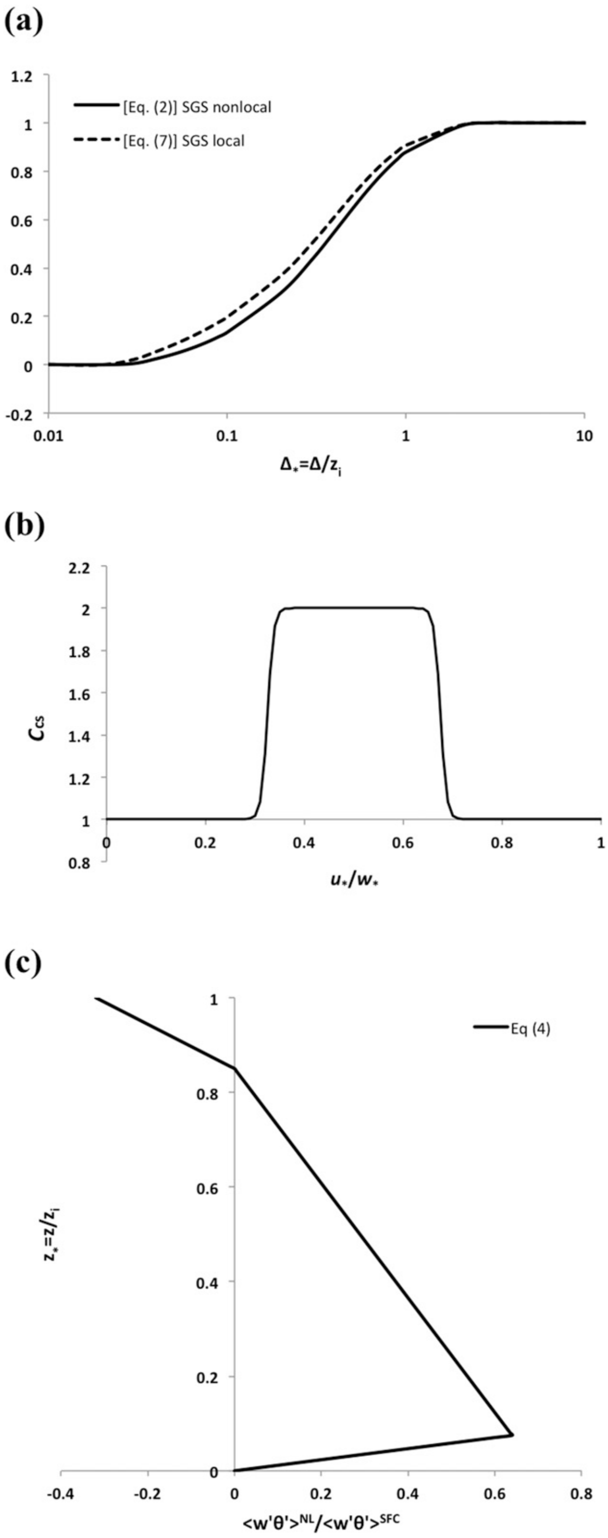

FIG. 2. (a) Grid-size dependency functions for SGS nonlocal [$P_{\mathrm{NL}}(\Delta_{*\mathrm{cs}})$ for $C_{\mathrm{cs}} = 1$: solid, Eq. (2)] and local [$P_L(\Delta_*)$: dotted, Eq. (7)] vertical heat transports, (b) stability dependency function [C_{cs}: Eq. (3)], and (c) total nonlocal vertical heat transport profile [Eq. (4)].

- For $u_*/w_* < 0.25$: $C_{\mathrm{cs}} = 1.0$ (a condition for thermal circulations, horizontal size of $1.0-1.5z_i$).
- For $0.35 < u_*/w_* < 0.65$: $C_{\mathrm{cs}} = 2.0$ (a condition for convective rolls, horizontal size of $2-3z_i$).
- For $u_*/w_* > 0.75$: $C_{\mathrm{cs}} = 1.0$ (a condition for streaky structures).
- C_{cs} has a smooth transition between the intervals.

The resultant coefficients are as follows: $a_{\mathrm{cs}} = 0.5$, $b_{\mathrm{cs}} = -40.0$, $c_{\mathrm{cs}} = -0.5$, $d_{\mathrm{cs}} = 8.0$, and $e_{\mathrm{cs}} = 3.0$. By including the stability effects, $P_{\mathrm{NL}}(\Delta_{*\mathrm{cs}})$ has a smaller value in the roll circulation case than in the thermal circulation case at the same grid mesh, which is consistent with the finding by SH13.

The nonlocal transport profile ($\langle w'\theta'\rangle^{\mathrm{NL}}$) (Fig. 2c) is designed to fit the domain-averaged LES profile (i.e., the transport profile for $\Delta = 8000$ m shown in Fig. 1a) and is composed of three physical parts: surface-layer cooling, mixed-layer heating, and entrainment. Each part is expressed by a linear function of z_* ($z_* \equiv z/z_i$):

$$\langle w'\theta'\rangle^{\mathrm{NL}} = \begin{cases} \langle w'\theta'\rangle^{\mathrm{NL}}_{\mathrm{SL}} = A_1 z_* + B_1: & 0.0 \le z_* \le \delta_{*\mathrm{SL}} \\ \langle w'\theta'\rangle^{\mathrm{NL}}_{\mathrm{ML}} = A_2 z_* + B_2: & \delta_{*\mathrm{SL}} \le z_* \le 1.0 - \delta_{*\mathrm{EZ}} \\ \langle w'\theta'\rangle^{\mathrm{NL}}_{\mathrm{EZ}} = A_3 z_* + B_3: & 1.0 - \delta_{*\mathrm{EZ}} \le z_* \le 1.0 \end{cases}. \tag{4}$$

Here $\delta_{*\mathrm{SL}} = 0.075$ is used, from Fig. 1a. The variable $\delta_{*\mathrm{EZ}} \equiv \delta_{\mathrm{EZ}}/z_i$, where δ_{EZ} is the thickness of the entrainment zone. The thickness of the entrainment zone is estimated according to Deardorff et al. (1980), with modified coefficients by Noh et al. (2003): $\delta_{\mathrm{EZ}}/z_i = d_1 + d_2\mathrm{Ri}_*^{-1}$. The quantities $d_1 = 0.02$ and $d_2 = 0.05$. The term $\mathrm{Ri}_* = (g/T_0)z_i\Delta\theta/w_m^2$ is the convective Richardson number. Note that although the entrainment layer depth is a key parameter in modeling the boundary layer, there is no universally accepted definition of the entrainment zone (Brooks and Fowler 2012), and its parameterization is highly questionable. Despite the uncertainty, we select the Deardorff's method as it has been used and evaluated in several models (Noh et al. 2003; Kim et al. 2006).

The coefficients A_{1-3} and B_{1-3} in Eq. (4) are determined as below.

- From Fig. 1a, $B_1 = 0$:
- $\langle w'\theta'\rangle^{\mathrm{NL}}_{\mathrm{SL}}(z_* = \delta_{*\mathrm{SL}}) = A_1\delta_{*\mathrm{SL}} = \langle w'\theta'\rangle^{\mathrm{NL}}_{\mathrm{ML}}(z_* = \delta_{*\mathrm{SL}})$; $A_1 = \langle w'\theta'\rangle^{\mathrm{NL}}_{\mathrm{ML}}(z_* = \delta_{*\mathrm{SL}})/\delta_{*\mathrm{SL}}$.
- $\langle w'\theta'\rangle^{\mathrm{NL}}_{\mathrm{ML}}(z_* = \delta_{*\mathrm{SL}}) = A_2\delta_{*\mathrm{SL}} + B_2$

  $\langle w'\theta'\rangle^{\mathrm{NL}}_{\mathrm{ML}}(z_* = 1.0 - \delta_{*\mathrm{EZ}}) = A_2(1.0 - \delta_{*\mathrm{EZ}}) + B_2 = 0.0$;

$$\begin{bmatrix} A_2 \\ B_2 \end{bmatrix} = \begin{bmatrix} \delta_{*\mathrm{SL}} & 1.0 \\ 1.0 - \delta_{*\mathrm{EZ}} & 1.0 \end{bmatrix}^{-1} \begin{bmatrix} \langle w'\theta'\rangle^{\mathrm{NL}}_{\mathrm{ML}}(z_* = \delta_{*\mathrm{SL}}) \\ 0.0 \end{bmatrix}$$

- $\langle w'\theta'\rangle^{\mathrm{NL}}_{\mathrm{EZ}}(z_* = 1.0 - \delta_{*\mathrm{EZ}}) = A_3(1.0 - \delta_{*\mathrm{EZ}}) + B_3 = 0.0$
  $\langle w'\theta'\rangle^{\mathrm{NL}}_{\mathrm{EZ}}(z_* = 1.0) = A_3 + B_3 = A_{R,\mathrm{NL}}\langle w'\theta'\rangle_{\mathrm{SFC}}$;
  $$\begin{bmatrix} A_3 \\ B_3 \end{bmatrix} = \begin{bmatrix} 1.0 - \delta_{*\mathrm{EZ}} & 1.0 \\ 1.0 & 1.0 \end{bmatrix}^{-1} \cdot \begin{bmatrix} 0.0 \\ A_{R,\mathrm{NL}}\langle w'\theta'\rangle_{\mathrm{SFC}} \end{bmatrix}.$$

To close the system, $\langle w'\theta'\rangle^{\mathrm{NL}}_{\mathrm{ML}}$ $(z_* = \delta_{*\mathrm{SL}})$ and $A_{R,\mathrm{NL}} \equiv \langle w'\theta'\rangle^{\mathrm{NL}}_{\mathrm{EZ}}(z_* = 1.0)/\langle w'\theta'\rangle_{\mathrm{SFC}}$ must be predetermined. Lenschow (1974) suggested that $\langle w'\theta'\rangle_{\mathrm{ML}}(z_*)/\langle w'\theta'\rangle_{\mathrm{SFC}} = 1.0 - 1.15z_*$ for $0 < z_* \le 0.87$. We define $f_{\mathrm{nl}} \equiv \langle w'\theta'\rangle^{\mathrm{NL}}_{\mathrm{ML}}(z_*)/\langle w'\theta'\rangle_{\mathrm{ML}}(z_*)$, which is the ratio of nonlocal heat flux to total heat flux, and set $f_{\mathrm{nl}} = 0.7$ in accordance with SH13 (cf. their Fig. 7). Then, $\langle w'\theta'\rangle^{\mathrm{NL}}_{\mathrm{ML}}(z_* = \delta_{*\mathrm{SL}})$ is determined. Note that f_{nl} could be a variable rather than a constant (LeMone 1976; Young 1988; Couvreux et al. 2010), while there is no established value for f_{nl} yet.

The variable $A_{R,\mathrm{NL}}$ can be estimated as proportional to the entrainment flux ratio A_R $[A_R \equiv \langle w'\theta'\rangle(z_* = 1.0)/\langle w'\theta'\rangle_{\mathrm{SFC}}]$: $A_{R,\mathrm{NL}} = f_{\mathrm{ent}}A_R$, and $f_{\mathrm{ent}} = A_{R,\mathrm{NL}}/A_R = 2.0$ is from an empirical fitting. For computing A_R, the method suggested by Conzemius and Fedorovich (2006b) is used:

$$A_R = \frac{w_m^3}{w_*^3}\,\frac{0.2}{1 - 0.4\mathrm{Ri}_{\mathrm{GS}}^{-1}}. \tag{5}$$

Here w_m is a combined turbulence velocity scale that includes both shear and buoyancy effects (Moeng and Sullivan 1994): $w_m^3 = w_*^3 + 5u_*^3$. The quantity $\mathrm{Ri}_{\mathrm{GS}}$ is the Richardson number associated with the entrainment zone shear. This method [Eq. (5)] considers surface- and entrainment-layer wind shear, as well as the surface fluxes. Via the grid-size dependency function $[P_{\mathrm{NL}}(\Delta_{*\mathrm{cs}})]$ and the nonlocal entrainment flux ratio $(A_{R,\mathrm{NL}})$, the prescribed profile includes the effects of surface and entrainment-layer wind shear as well as the surface fluxes, while being still limited to dry CBLs and not covering moist convection situations (e.g., cloudy boundary layers).

Note that the prescribed nonlocal transport profile is a complete change from the nonlocal term in the K-profile models. That is, $\langle w'\theta'\rangle^{S(\Delta_*),\mathrm{NL}}$ in Eq. (1) replaces the sum of $K_H\gamma_H$ and the explicit entrainment term in the Yonsei University (YSU) model (Hong et al. 2006), or replaces $K_H\gamma_H$ in the models by Troen and Mahrt (1986) and Holtslag and Boville (1993). The variable K_H is the vertical diffusivity for heat, and γ_H is the gradient-adjustment term for heat. As will be shown in section 3a, the traditional nonlocal term does not well describe the updrafts-induced vertical heat transport profiles.

b. Local heat transport

The local heat transport is parameterized, using the eddy-diffusivity formulation. An explicit grid-size-dependent function, $P_L(\Delta_*)$ (Fig. 2a), is considered in computing the vertical diffusivity (K_H), in order to suppress the parameterized transport as grid size decreases:

$$\langle w'\theta'\rangle^{S(\Delta_*),L} = -K_H(\Delta_*)\frac{\partial\overline{\theta}^{\Delta}}{\partial z} = -K_{H,\mathrm{PBL}}P_L(\Delta_*)\frac{\partial\overline{\theta}^{\Delta}}{\partial z}, \tag{6}$$

$$P_L(\Delta_*) = 0.280\frac{(\Delta_*)^2 + 0.870(\Delta_*)^{1/2} - 0.913}{(\Delta_*)^2 + 0.153(\Delta_*)^{1/2} + 0.278} + 0.720. \tag{7}$$

In Eq. (6), the superscript L and subscript H refer to local and heat, respectively. The stability function (C_{cs}) is not used in the local transport, since SH13 showed that the CBL stability mainly changes the resolution dependency of the nonlocal transport, and its effects on the local part are relatively small. The variable $K_{H,\mathrm{PBL}}$ is the vertical diffusivity used in the conventional PBL parameterization.

Here, we select the prescribed K-profile in the YSU PBL scheme (Hong et al. 2006) as $K_{H,\mathrm{PBL}}$:

$$K_{H,\mathrm{PBL}} = \kappa w_s z\left(1 - \frac{z}{h}\right)^2, \tag{8}$$

where κ is the von Kármán constant (0.4), and w_s is the mixed-layer velocity scale. The variable h is the PBL height used in the YSU PBL scheme, and the bulk Richardson number is zero at h.

The model calculates an appropriate amount of the SGS transport for the typical LES grid sizes [i.e., $P_{\mathrm{NL}} \sim 0.04$ and $P_L \sim 0.08$, for $\Delta_* = 0.05$ and $C_{\mathrm{cs}} = 1$], even though the model is not based on the isotropic turbulence theory in the LES limit. On the other hand, the SGS transport in the model becomes zero as $\Delta_* < 0.025$, rather than converging to that of LES, because the grid-size dependency functions $[P_{\mathrm{NL}}$ and $P_L]$ approach zero at the limit (cf. Fig. 2a). An ideal gray-zone parameterization may have a smooth transition from a one-dimensional PBL parameterization to a three-dimensional LES SGS model, not only in terms of the amount of the SGS transport, but also the formula, while the dimension issue (transition from 1D to 3D) and the numerical diffusion issue (horizontal diffusion based on physical versus numerical reasons) complicate the problem. There was an attempt to blend a 1D PBL parameterization and the vertical diffusion part of an LES SGS model, by blending their length scales (Boutle et al. 2014), while the dimension and numerical issues still remain unsolved.

TABLE 1. Boundary layer statistics at $2t_0$ [$t_0 = 6\tau_*$ is the time required for the dynamic flow field to reach a statistically quasi-equilibrium state (Moeng and Sullivan 1994)] for the benchmark LES.

	$\overline{w'\theta'}_{\mathrm{SFC}}$ (K m s^{-1})	U_g (m s^{-1})	w_* (m s^{-1})	u_* (m s^{-1})	z_i (m)	τ_* (s)	L_{MO} (m)
BF	0.20	10	1.864	0.518	996.98	535	−53.65
SW	0.05	10	1.152	0.481	937.97	815	−170.94

3. Evaluation

a. Idealized simulations

1) MODEL SETUP

Four CBL cases in SH13 are simulated for 4 h using the new algorithm at $\Delta = 250$, 500, and 1000 m, and the results of two cases among them—the cases forced by $(\overline{w'\theta'}_{\mathrm{SFC}}, U_g) = (0.20\,\mathrm{K\,m\,s^{-1}}, 10.0\,\mathrm{m\,s^{-1}})$ [the buoyancy driven (B) as well as wind forced (F) (BF) case in SH13] and $(\overline{w'\theta'}_{\mathrm{SFC}}, U_g) = (0.05\,\mathrm{K\,m\,s^{-1}}, 10.0\,\mathrm{m\,s^{-1}})$ [the weaker-shear (SW) case in SH13]—are presented in this study. The CBL stability parameter, u_*/w_*, is 0.27 for the BF and 0.41 for the SW, and the SW case meets the conditions for the appearance of the horizontal convective rolls (Moeng and Sullivan 1994). The results for the other two cases (i.e., the BT and SS cases in SH13) are similar to those for BF and SW simulations, and not presented here [cf. the BT case is buoyancy driven (B), and organized thermals (T) appear; the SS case is the stronger-shear case]. Boundary layer statistics for the benchmark LES runs are summarized in Table 1.

The Weather Research and Forecasting (WRF) Model (Skamarock et al. 2008) is used for the simulations. The experimental setup is identical to the benchmark LES setup (the appendix), except for the SGS vertical diffusion scheme and horizontal resolution (cf. Table 2). In the WRF model, the third-order Runge–Kutta time integration scheme is used for the temporal discretization of the governing equations for low-frequency modes, and a time-split integration scheme is adopted for high-frequency modes. For the spatial discretization, the fifth-order (third order) accurate finite-differencing advection scheme is applied for horizontal (vertical) advection, and an Arakawa C-grid system is used. The domain size is $8^2\,\mathrm{km}^2$ for the numerical simulations with $\Delta = 250$ m, as in the benchmark LES (Table 2 and the appendix). The domain size is enlarged to 16^2 and $32^2\,\mathrm{km}^2$ for the simulations with $\Delta = 500$ and 1000 m, in order to make the simulation domain sufficiently larger than the corresponding effective resolution [6–7Δ, in Skamarock (2004)]. To compare the performance of the new algorithm with that of a conventional *K*-profile PBL model, the YSU experiment is also conducted; the YSU PBL parameterization (Hong et al. 2006) is used as the vertical mixing algorithm for all resolutions. The three-dimensional TKE-based SGS model (Deardorff 1980) is used for horizontal diffusion, in addition to the one-dimensional PBL scheme for vertical diffusion. Important features of each experiment are summarized in Table 2.

The simulation results are evaluated in comparison with the reference data (hereafter REF) for the periods t_0–$3t_0$, not otherwise specified. Here $t_0 = 6\tau_*$ (τ_*: the large-eddy turnover time) is the time required for the dynamic flow field of the benchmark LES runs to reach a statistically quasi-equilibrium state (Moeng and Sullivan 1994). The variable t_0 is roughly 3600 and 5400 s for the BF and SW cases, respectively. Note that in the idealized simulations and section 3a, u is the wind parallel to U_g.

2) TEMPERATURE AND HEAT TRANSPORT PROFILES

Figure 3 shows the simulated potential temperature profiles for the NEW and YSU experiments. The NEW experiment reproduces the LES profiles well (Figs. 3a,c) except for the small differences between the resolutions near z_i at t_0, while the differences almost disappear at $3t_0$. The YSU PBL scheme is less dependent on Δ (Figs. 3b,d) because the scheme is designed for parameterizing the total transport profile regardless of Δ (cf. Fig. 4d). The stability in the upper mixed layer is weaker and more realistic in the NEW experiment, while the YSU PBL overestimates the sharpness of the profile near the top of the boundary layer. The improvement in the mean profiles by the new algorithm is mainly due to the

TABLE 2. Summary of vertical and horizontal SGS turbulence models, vertical and horizontal grid size, number of horizontal grids, and horizontal domain size for the benchmark LES, reference data (REF), and NEW and YSU experiments.

	Vertical SGS	Horizontal SGS	Vertical grid size (m)	Horizontal grid size (m)	No. of grids	Domain size (km^2)
Benchmark LES	3D TKE	3D TKE	20	25	320^2	8^2
Reference (REF)	Filtered from the LES		20	250, 500, 1000	32^2,16^2, 8^2	8^2
NEW	NEW	3D TKE	20	250, 500, 1000	32^2	8^2, 16^2, 32^2*
YSU	YSU	3D TKE	20	250, 500, 1000	32^2	8^2, 16^2, 32^2*

* Domain size is extended to 16^2 and $32^2\,\mathrm{km}^2$ for $\Delta = 500$ and 1000 m, respectively.

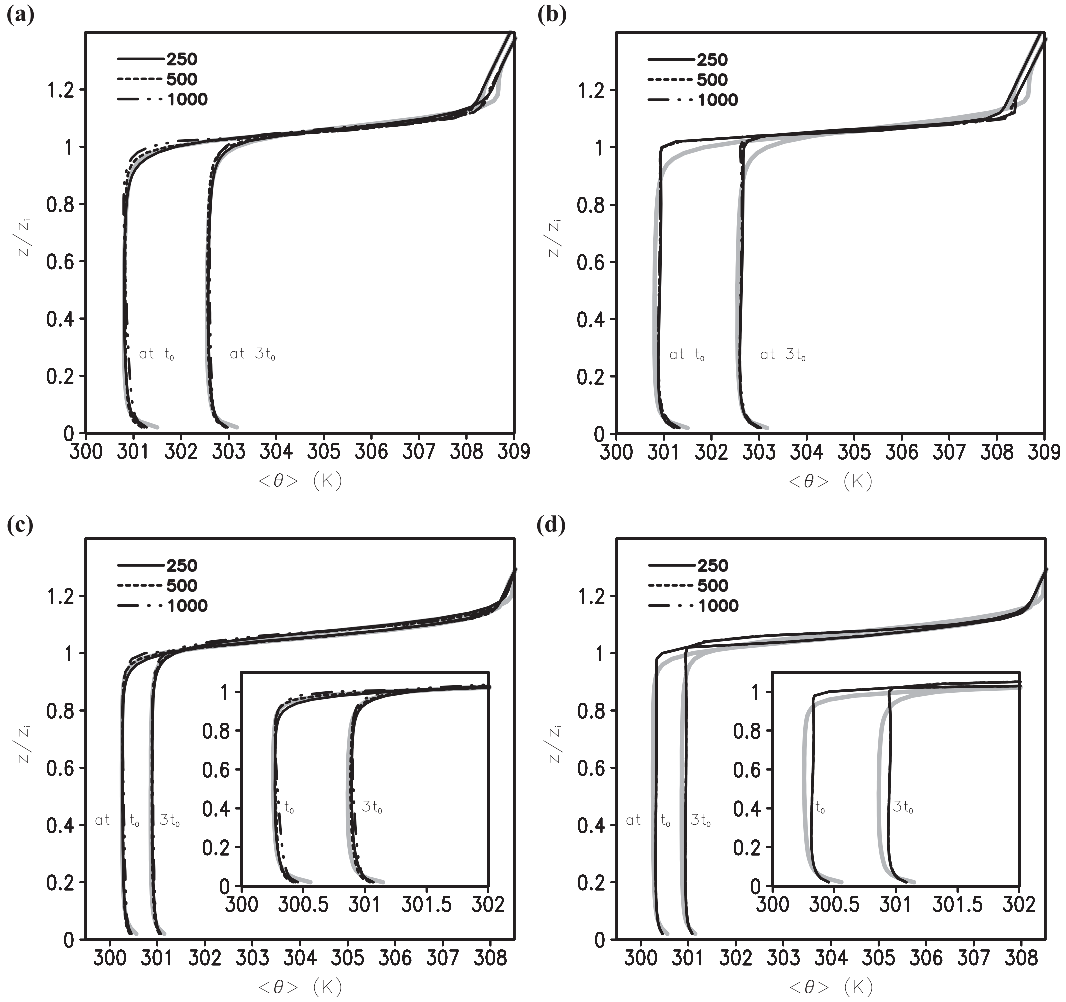

FIG. 3. Domain-averaged potential temperature profiles for (left) NEW and (right) YSU experiments for cases (a),(b) BF and (c),(d) SW, with corresponding REF profiles (solid gray): $\Delta = 250$ m (solid black), 500 m (dotted black), and 1000 m (dot–dot–dashed black). In (c) and (d), each inset provides a closer look at the corresponding temperature profile.

‘‘total’’ nonlocal transport profile fit to the LES data [Eq. (4)] rather than to the inclusion of the grid-size dependency function, in that the improvement appears also at $\Delta = 1000$ m where the amount of the SGS transport is comparable to the total transport (cf. Fig. 1).

The total heat transport and its separation into the resolved and SGS parts are shown in Fig. 4, for the case BF. The new method calculates the SGS heat transport similar to that in the reference (Fig. 4a), despite its simplicity. The algorithm slightly underestimates the SGS flux in the PBL, but the overestimation of the resolved vertical transport compensates for the shortage (Figs. 4b, c). In the entrainment zone as the SGS transport reduces via the grid-size dependency functions the resolved transport becomes larger, which is consistent with the reference. The YSU scheme also reproduces the reference total heat flux (Fig. 4f), but the SGS (Fig. 4d) and resolved (Fig. 4e) transports are only slightly dependent on the resolution and do not follow the reference data. The YSU scheme parameterizes all the heat transport regardless of the resolution, suppressing the resolved motions (cf. LeMone et al. 2013; Ching et al. 2014).

The SGS transport profile is composed of nonlocal and local components (Fig. 5). The NEW experiment reproduces the basic role of the nonlocal transport (i.e., surface-layer cooling, mixed-layer heating, and entrainment; Fig. 5a) because the simple profile is designed to imitate it (cf. section 2a). However, the magnitude of the flux is underestimated in the surface layer and entrainment zone, and slightly overestimated in the mixed layer. The local flux makes up for the defects of the nonlocal

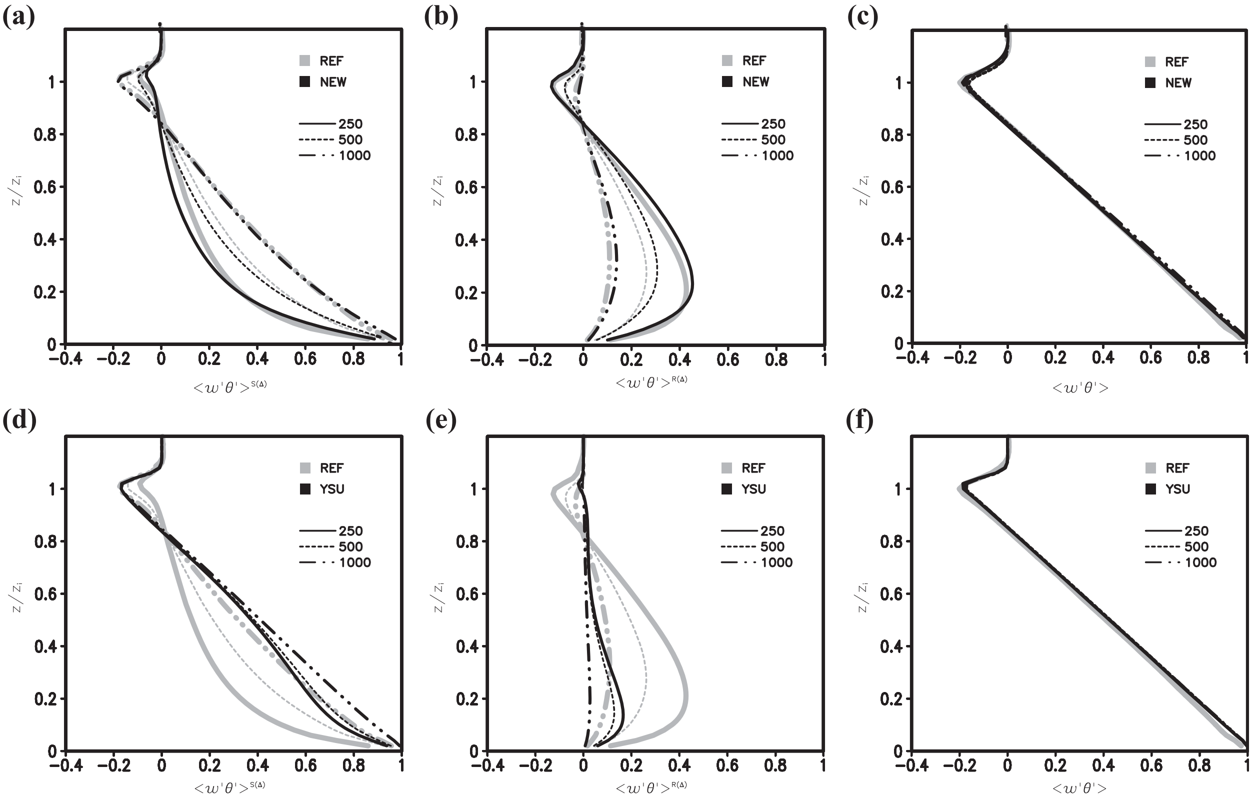

FIG. 4. For case BF, domain-averaged (a),(d) subgrid-scale (SGS); (b),(e) resolved; and (c),(f) total vertical heat transport profiles for (top) NEW and (bottom) YSU experiments (black) with corresponding REF profiles (gray): $\Delta = 250$ m (solid), 500 m (dotted), and 1000 m (dot–dot–dashed).

part (Fig. 5b) while maintaining its role of heating the boundary layer [i.e., $-\partial\langle w'\theta'\rangle^{S(\Delta_*),L}/\partial z > 0$ roughly up to z_i in both REF and NEW]. The local flux near the PBL top is an exception; the local flux from the NEW experiment has negative values while that from the REF has positive values. Several studies showed that the heat flux by the small-scale turbulence is not always negative in the entrainment layer (Kaiser and Fedorovich 1998; Hellsten and Zilitinkevich 2013), while its representation via the eddy-diffusivity formula always results in the negative flux by definition. The reference local transport profile is consistent with the two studies (e.g., Figs. 5b,d), whereas there are also many studies showing the negative heat flux by the small-scale turbulence in the entrainment layer. It is worth noting that as SH13 mentioned the conditional sampling method used for separating nonlocal and local transports only consider updrafts and have limitations especially for variables that are largely affected by the organized entrainment events.

The nonlocal term in the YSU PBL scheme (i.e., the gamma term) does not follow the reference data (Fig. 5c). It calculates cooling from the surface to the middle of the CBL (i.e., $-\partial\langle w'\theta'\rangle^{S(\Delta_*),\mathrm{NL}}/\partial z < 0$), whereas the cooling by the NL transport is limited to the surface layer in the REF. This results in the local component from the YSU model having the larger heating up to the middle of the CBL, while the amount of heating decreases above the surface layer in the REF (Fig. 5d).

Figure 6 shows the SGS heat transport and its separation into the nonlocal and local parts for the SW case, in which the relative importance of wind shear (i.e., u_*/w_*) is larger than in the BF case (cf. Table 2). The reference profile indicates the larger entrainment flux ratio as revealed by previous studies (Kim et al. 2003; Angevine 2005; Conzemius and Fedorovich 2006a), and the NEW experiment well reproduces it. On the other hand, the SGS transport is more underestimated in the mixed layer and overestimated in the surface layer compared to the BF case (cf. Figs. 6a and 4a), and this is in line with the errors in the local transport (Fig. 6c). In the SW case, there is almost no resolved transport in the YSU experiment, because the YSU PBL scheme parameterizes almost all the heat transport (not shown, but very similar to Figs. 4d–f and Figs. 5c,d).

Figure 7 presents the grid-size dependence of the total (black), resolved (red), and SGS (blue) vertical heat transports in the PBL. Note that the NEW and YSU results are normalized by the reference total (resolved

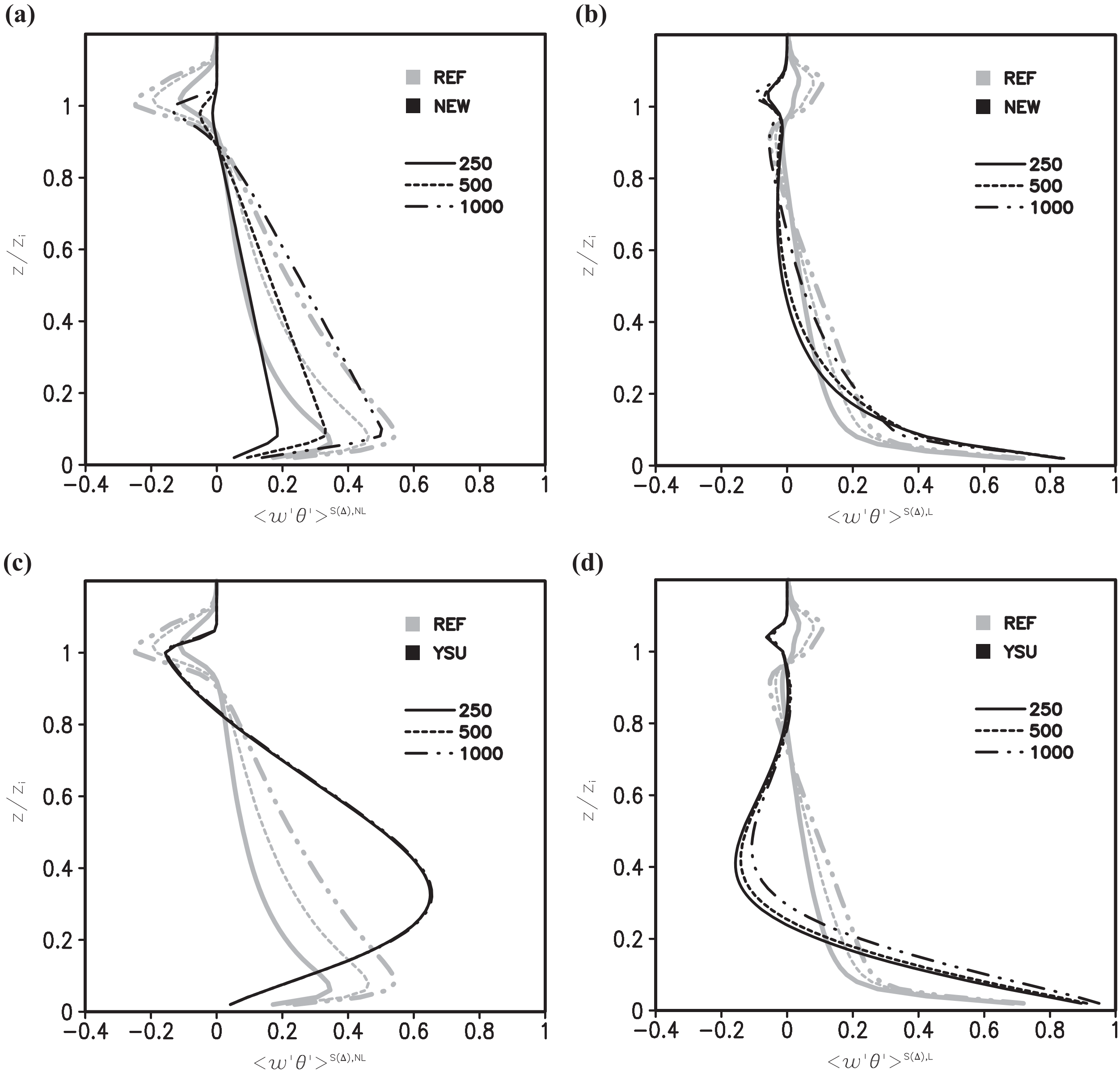

FIG. 5. As in Fig. 4, but for (a),(c) SGS nonlocal and (b),(d) SGS local vertical heat transport profiles.

plus SGS) transport. The reference total transport does not vary by grid resolution. For the BF case (Figs. 7a–c) the NEW experiment well reproduces the grid-size dependency derived from the reference data, while the model slightly underestimates the SGS partition in the mixed layer at $\Delta = 250$ m and $\Delta = 500$ m (Fig. 7b) and overestimates it in the entrainment zone at $\Delta = 1000$ m (Fig. 7c). The new model also well follows the reference data for the SW (Figs. 7d–f), except for the overestimated SGS transport in the surface layer at all three resolutions (Fig. 7d) and in the upper layers at $\Delta = 1000$ m (Figs. 7e,f). Despite the shortcomings, the new algorithm improves the modeled grid-size dependency compared to the YSU scheme. For both BF and SW cases, the YSU scheme shows large positive biases in the computed SGS partition, and its grid-size dependency is small. This is consistent with the performance of an eddy-diffusivity mass flux (EDMF) scheme (Pergaud et al. 2009) evaluated by Honnert et al. (2011). Honnert et al. showed that the ratio of the parameterized SGS TKE calculated by the EDMF scheme is almost 1 for $\Delta_* = 1$ and 0.8 for $\Delta_* = 0.25$ [cf. Fig. 14f in Honnert et al. (2011)], very similar to the ratio calculated by the YSU PBL scheme. They also revealed that the resolved energy and transport do not dominate the corresponding parameterized parts in the gray zone regardless of the

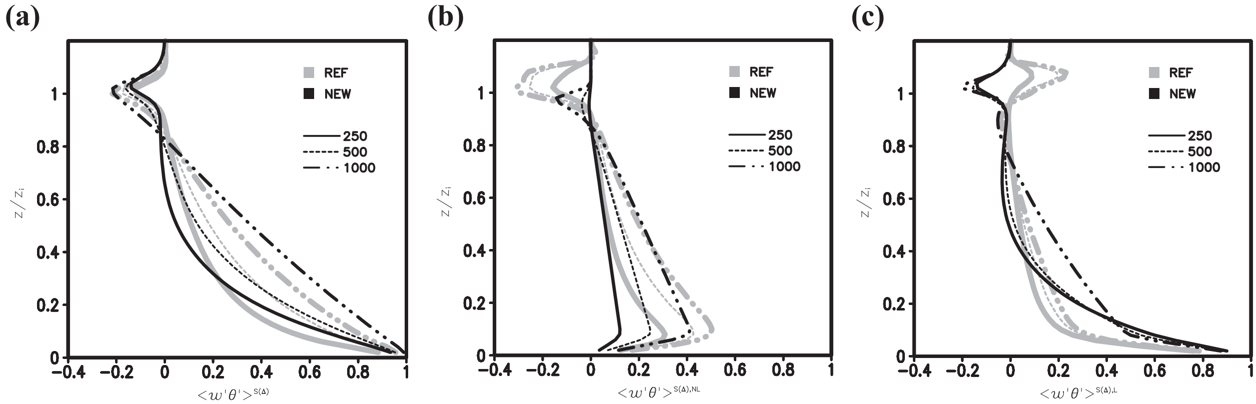

FIG. 6. As in Fig. 4, but for case SW, domain-averaged (a) subgrid-scale (SGS), (b) SGS nonlocal, and (c) SGS local vertical heat transport profiles for only NEW experiment (black).

length scale used in computing the eddy diffusivity, within the EDMF scheme framework they used.

3) ENERGY SPECTRUM AND HORIZONTAL VARIANCES

To further investigate the ability of the PBL models to accurately resolve dry convection at various scales and to dissipate small-scale motions, two-dimensional energy spectra are calculated (Figs. 8 and 9). The NEW and YSU simulations are affected by an implicit sixth-order numerical diffusion due to the fifth-order horizontal advection scheme used (cf. Skamarock 2004). For a better comparison with the simulations, the reference fields are filtered by a sixth-order numerical filter before computing the spectra.

Figure 8 presents the two-dimensional spectra for the BF case. For $\Delta = 250$ m, the energy spectra from the NEW experiment follow the reference w spectra in the mixed layer well, while the YSU scheme removes too much energy (Figs. 8a,d). Note that the large-eddy simulation for the BF case reaches a quasi-equilibrium state at t_0. The NEW experiment also reaches an equilibrium state roughly at t_0, whereas the YSU experiment has a local energy peak near the smallest resolved scales (Fig. 8a). At $\Delta = 500$ m and $\Delta = 1000$ m, both NEW and YSU simulations show local energy peaks near $\lambda = 2\Delta$ for the t_0–$3t_0$ periods (Figs. 8b,c), whereas the energy peaks move to larger scales for the $3t_0$–$4t_0$ periods (Figs. 8e,f). This is because the energy peaks of the numerical experiments for $\Delta = 500$ m and $\Delta = 1000$ m continue to move to larger scales after t_0 and approach a quasi-equilibrium state roughly at $2t_0$ and $3t_0$, respectively (not shown). Note that Ching et al. (2014) demonstrated that the growth rate of perturbations is inversely proportional to grid size (smallest resolved scales), because the superadiabatic layer in the lower CBL allows generation of modeled convectively induced secondary circulations (M-CISCs). The different time for reaching an equilibrium state according the resolution in our results also indicates the grid-size-dependent growth rate of the perturbations. This indicates that the M-CISCs and the accompanying spinup problem remain unsolved at gray-zone resolutions in the NEW experiment, even though resolution dependency is considered in the algorithm.

After reaching the equilibrium state, the results from the NEW experiment show an improvement over those from the YSU experiment at $\Delta = 500$ m (Fig. 8e), but the energy is still weakly underestimated at almost all relevant scales. Compared to the spectrum for the finer-resolution simulations, the energy spectrum for the 1000-m resolution is less affected by the vertical transport algorithm at small scales (Fig. 8f). At that resolution, the SGS transport is comparable to the total transport (cf. Figs. 1 and 7), and the grid-size dependency function approaches 1 (cf. Fig. 2a). Therefore, the differences between the NEW and YSU experiments are mainly from the total nonlocal transport profile, rather than from the inclusion of the scale dependency. Moreover, the spectral peak scale (1–$2z_i$) is below the effective resolution (6–7Δ) for $\Delta = 1000$ m (cf. Skamarock 2004), and the numerical diffusion by the fifth-order horizontal advection scheme dominates the energy spectrum, resulting in a smaller contribution from the SGS parameterization except for the scales larger than the effective resolution.

The two-dimensional spectra for the SW case are shown in Fig. 9. Compared to the BF case (cf. Fig. 8), the YSU scheme underestimates the resolved energy even more in the case (note that the scale on the y axis is different between Figs. 8 and 9). This figure confirms the improvement in resolved motions by the new model in different stability conditions, even though the resolved energy is still underestimated at $\Delta = 1000$ m (Fig. 9c).

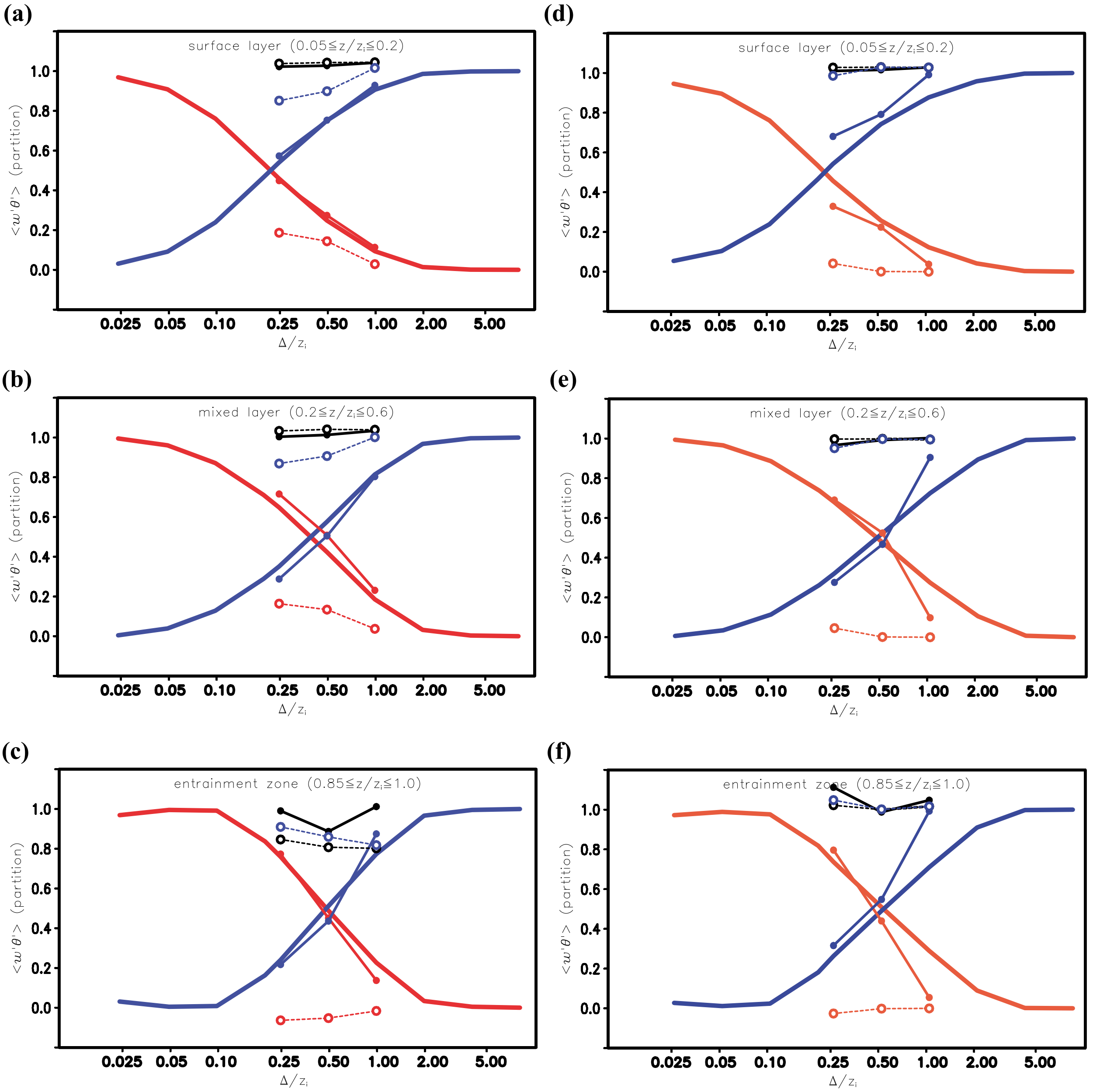

FIG. 7. For cases (left) BF and (right) SW, grid-size dependence of the total (black), resolved (red), and SGS (blue) vertical heat transports normalized by the REF total transport for NEW (solid with closed circles) and YSU (dotted with open circles) experiments with corresponding references (solid without marks). Results are shown for the (a),(d) surface layer; (b),(e) mixed layer; and (c),(f) entrainment zone.

The resolved horizontal variances (e.g., $\langle w'^2\rangle$, $\langle \theta'^2\rangle$, and $\langle u'^2\rangle$) measure the horizontal variability, as well as the resolved energy ($\langle c'^2\rangle^{R(\Delta)} = \int_{\kappa_1=2\pi/D}^{\kappa_2=2\pi/\Delta} E_c(\kappa)\,d\kappa$, where D is the size of the simulation domain). The horizontal variability profiles of the NEW experiment well follow the reference profiles (Figs. 10a–c), while $\langle u'^2\rangle$ is underestimated in the mixed layer and $\langle w'^2\rangle$ and $\langle \theta'^2\rangle$ are slightly overestimated in the mixed layer and entrainment layer, respectively. Nevertheless, the variances are closer to those of the reference for all variables at all resolutions considered, compared to those for the YSU experiment (Figs. 10d–f).

The overall improvements in the energy spectra and variance profiles indicate that the resolved fields of the gray-zone simulations can be improved by reducing the SGS transport, given reasonable total nonlocal and local transport profiles and scale-dependency functions.

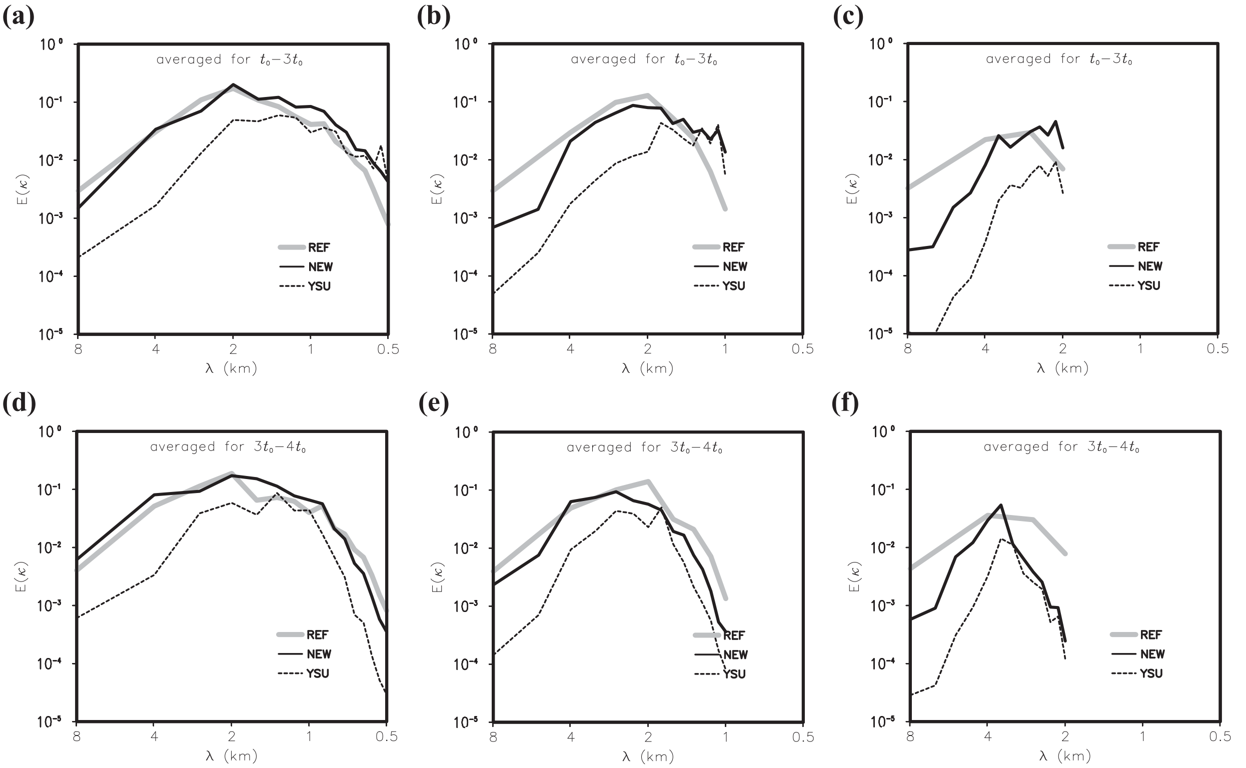

FIG. 8. For case BF, vertical velocity (w) spectra at $0.5z_i$ for (top) t_0-3t_0 and (bottom) $3t_0$–$4t_0$ periods from NEW (solid black) and YSU (dotted black) experiments with corresponding reference data (solid gray): (a),(d) $\Delta = 250$ m; (b),(e) 500 m; and (c),(f) 1000 m. The spectra for the benchmark LES and corresponding reference reach an equilibrium state at t_0, while the NEW and YSU experiments reach an equilibrium state roughly at t_0 for $\Delta = 250$ m, $2t_0$ for $\Delta = 500$ m, and $3t_0$ for $\Delta = 1000$ m.

4) WIND AND MOMENTUM TRANSPORT PROFILES

The momentum transport profile in the gray zone is computed by multiplying a scale-dependent function with the total momentum transport profile. The total transport profile is calculated according to the momentum transport algorithm implemented in the YSU PBL scheme (Hong et al. 2006). That is, the gamma term is kept for the total nonlocal momentum transport, while the term is replaced with the newly derived nonlocal transport profile for the heat transport [Eq. (4)]. Note that Frech and Mahrt (1995) mentioned that the gamma-type nonlocal momentum transport term cannot be formally justified, but the inadequacy of existing data does not allow improvement upon this gamma-type scheme (Mahrt and Gibson 1992; Frech and Mahrt 1995; Brown and Grant 1997).

Figure 11 shows that the SGS momentum transport decreases as Δ decreases in the NEW experiment,

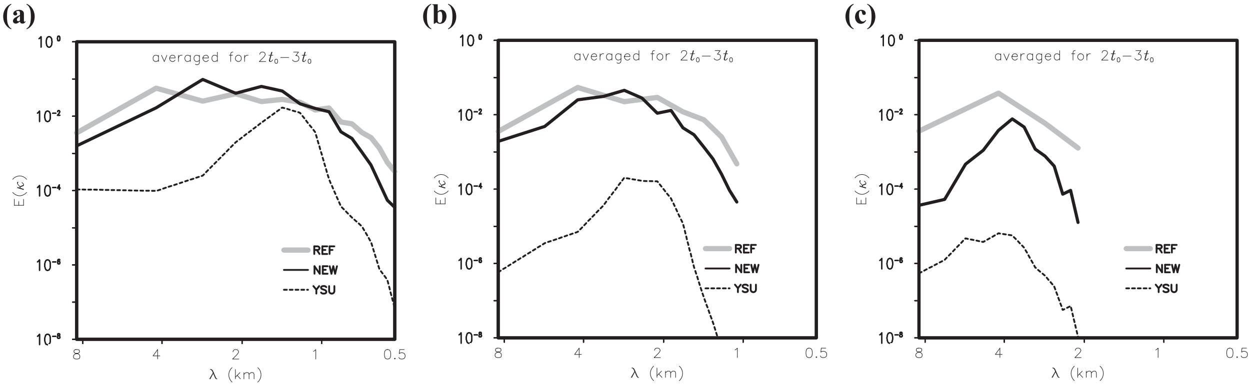

FIG. 9. As in Fig. 8, but for case SW during the period $2t_0$–$3t_0$.

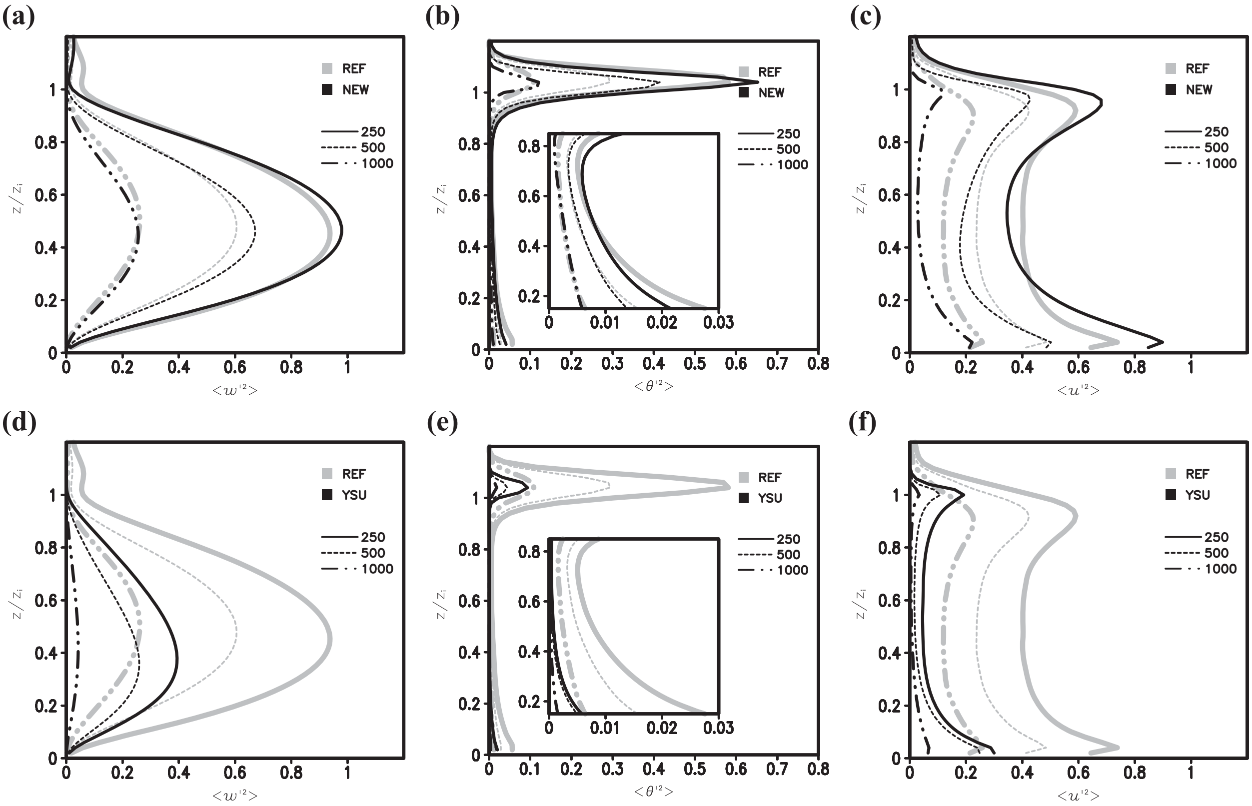

FIG. 10. For case BF, vertical profiles of resolved (a),(d) $\langle w'^2 \rangle$; (b),(e) $\langle \theta'^2 \rangle$; and (c),(f) $\langle u'^2 \rangle$ for (top) NEW and (bottom) YSU experiments (black), with corresponding REF profiles (gray): $\Delta = 250$ m (solid), 500 m (dotted), and 1000 m (dot–dot–dashed). In (b) and (e), each inset provides a closer look at the corresponding variance profile.

according to the inclusion of the grid-size function (Fig. 11a). The transport for the YSU experiment is only weakly sensitive to the resolution, except in the lower PBL (Fig. 11b). In spite of the improvement in the SGS momentum transport, the resulting wind profiles still deviate from the reference profiles (Fig. 11c). However, the wind profiles for the NEW algorithm are closer to the reference profile compared to the YSU profiles (Fig. 11d).

b. *Real-case simulations forced by analysis data*

1) CASE DESCRIPTION AND EXPERIMENTAL SETUP

To test the effects of the SGS transport algorithm in real case simulations, which are forced by analysis data, the 2002 International H_2O Project (IHOP_2002; Weckwerth et al. 2004) fair-weather CBL is simulated using the WRF Model version 3.5.1. L10 conducted numerical simulations of the fair-weather CBL using earlier versions of the WRF Model (versions 2.1.2 and 3.0) for four selected days in the IHOP_2002 period. They used an earlier version of the YSU PBL scheme (as in WRF version 3.0) for vertical transport. We select one of the days, 20 June 2002, when the roll structures were observed and for which L10 conducted several idealized sensitivity tests with respect to grid size, numerical filter, and surface boundary conditions. Their simulation at 1-km grid spacing produced convective rolls. However, sensitivity tests revealed that the results were accidental; reducing the grid size led to narrower roll spacing and more irregular convection. As the grid-size-dependent convective rolls seem to be partly caused by the PBL scheme used, we expect an improvement in the simulated roll structures by using the new method.

A 24-h simulation is conducted, initialized at 1200 UTC 20 June 2002 by the operational National Centers for Environmental Prediction (NCEP) Eta Model output (40-km resolution). Boundary conditions are forced by the same data every 6 h. We use the outermost domain (d01) with 9-km grid spacing (237 × 201) and three one-way nested domains (d02–d04; Fig. 12): 3 km (280 × 229), 1 km (391 × 229), and 333.3333 m (201 × 201) (hereafter, 333 m, rounded off to a whole number) grid spacing. The physics package used is the same as in L10, but there have been several updates in each physics scheme from the earlier version of WRF used in L10 to version 3.5.1.

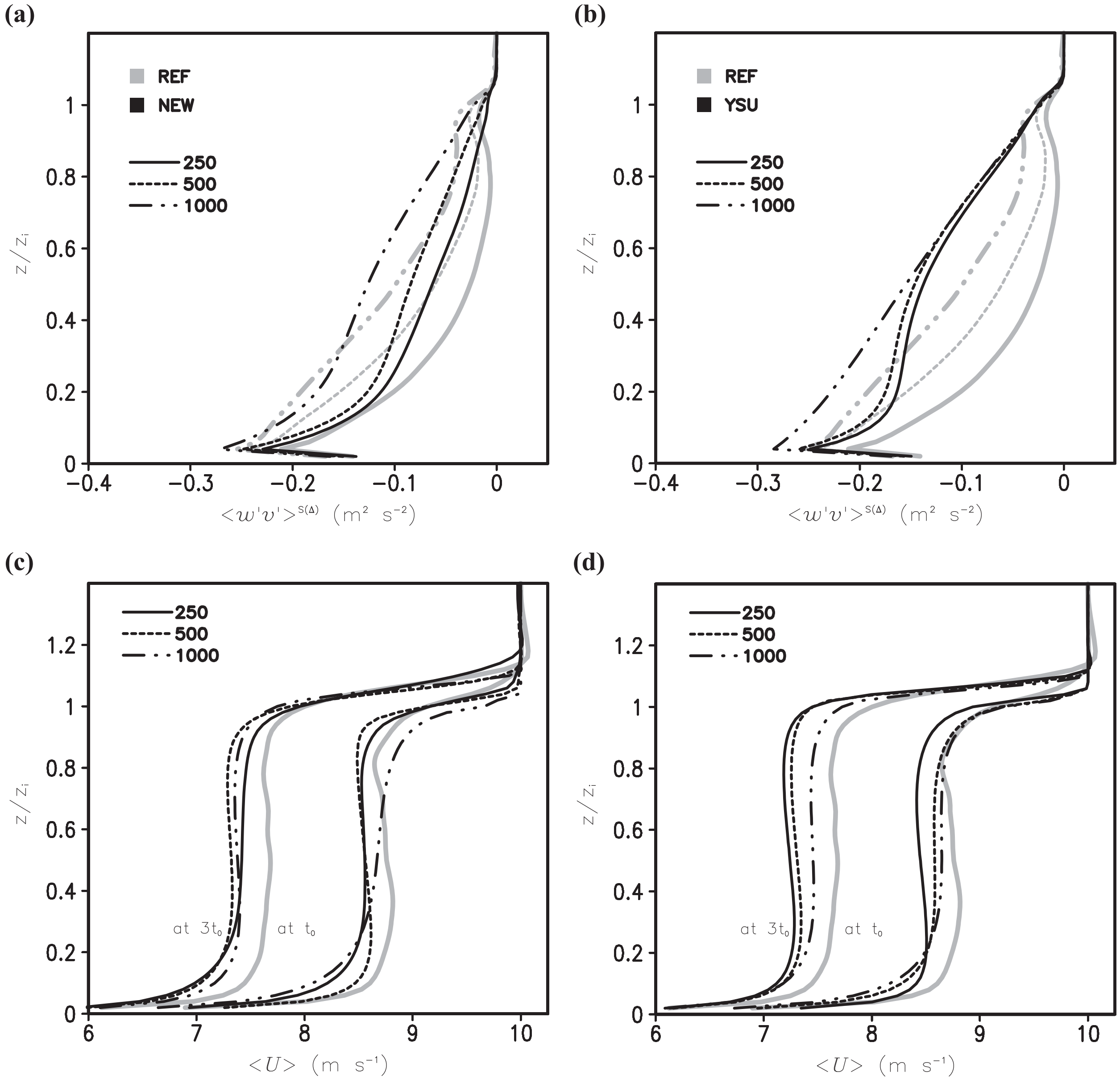

FIG. 11. For case BF, domain-averaged (top) SGS momentum transport and (bottom) momentum profiles for the (a),(c) NEW and (b),(d) YSU experiments (black), with corresponding REF profiles (gray): Δ = 250 m (solid), 500 m (dotted), and 1000 m (dot–dot–dashed).

2) RESULTS

For the real-case convective roll simulations in this subsection, we use a roll coordinate system with x axis along the rolls and y axis cross the rolls (cf. Fig. 13a). The along-roll wind is designated by u and the cross-roll wind is designated by v, as defined in roll studies (e.g., LeMone 1973). Note that this definition is different with the traditional wind directions in modeling studies, where u is the zonal wind.

Figure 13 shows the snapshot of simulated vertical velocity distributions over the d04 area (cf. Fig. 12) at the fifth model level (roughly at $z = 500$ m) at 1800 UTC 20 June 2002. The 1-km resolution runs simulate convective rolls in the south-southeast–north-northwest direction (Figs. 13a,c), as in L10. The modeled roll spacing is about 4–6 km [$\sim(3\text{–}4)z_i$] for both NEW and YSU experiments. Compared to the YSU experiment, the intensity of vertical motions, both updrafts and downdrafts, is strengthened in the NEW experiment. Results at $\Delta = 333$ m (Figs. 13b,d) are different from those of L10, whose idealized simulations showed that the modeled roll wavelength decreases and convection is more irregular and cellular with smaller grid size. The

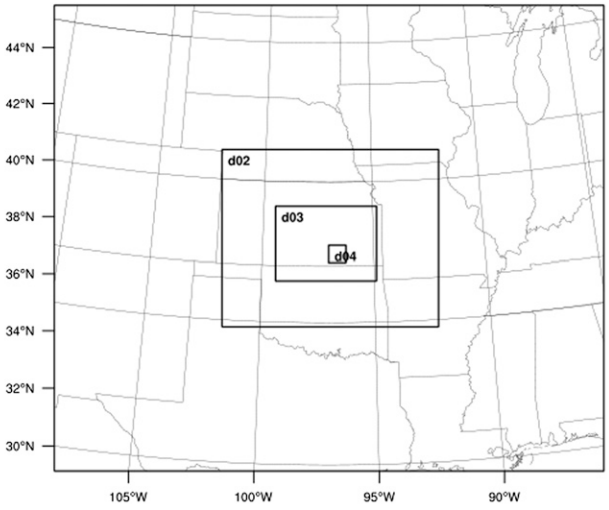

FIG. 12. Model domains for IHOP_2002 case simulations.

roll spacing in the 1-km NEW experiment is maintained in the 333-m NEW simulation with stronger vertical motions. In the 333-m YSU run, the convection in the downstream regions of the domain appears smaller and more irregular than the convection in the 1-km YSU run; however, the simulated convective rolls are larger and more organized than those in L10. We repeated the YSU experiment using the YSU PBL code in WRF version 3.0, and the results were between those in L10 and Fig. 13d (not shown). This indicates that the cellular convection that appeared at the 333- and 200-m YSU experiment in L10 is partly due to the PBL scheme used, while other major factors also influence the result (i.e., factors different from the experimental setup of this study, such as idealized initial and boundary conditions, surface forcing, nesting, and others). Determination of these factors is beyond the scope of this study.

Vertical cross sections of w and roll-scale cross-roll wind (v_r) along the cross line C1 (cf. Fig. 13a) are presented in Fig. 14. Here, the roll-scale wind (v_r) is simply calculated by subtracting d04-averaged v from each grid value, since it was shown that v energy is strongly concentrated in the roll frequency (LeMone 1973) and the lower-frequency motions are removed by subtracting the domain average. Figure 14 shows several typical features of convective rolls: the updrafts can be explained by the convergence of v and v reverses its direction near the roll top. As can be expected from Fig. 13, as well as from the idealized simulation results, the circulations are stronger in the NEW experiment (cf. Figs. 14a,c and 14b,d).

Figure 15 shows the vertical cross sections farther north, for the NEW experiment: along the cross lines C2 and C3 (cf. Fig. 13a). At $\Delta = 1000$ m, the roll spacing and roll circulations found along C1 are approximately kept in the farther downstream regions (cf. Fig. 14a and Figs. 15a,b). On the other hand, at $\Delta = 333$ m (Figs. 14b and 15c,d) the wide and regularly spaced updrafts along C1 split into the narrower and more irregular motions, especially along C3 (Fig. 15d). The updrafts are much narrower and unevenly distributed in the YSU experiment (not shown), as can be expected from Fig. 13.

This dependency of the convection structures on the distance from the inflow boundaries indicates the presence of the nesting effects. For neutral and weakly convective boundary layers Mirocha et al. (2014) showed that a nesting does not yield turbulence on the nested domain until some distance from the inflow boundaries. On the other hand, Park et al. (2014) found a significant reflection and distortion of the waves and accumulated noise in the downstream regions owing to the nesting, via their idealized baroclinic wave simulations. In the gray-zone simulations such as ours it is hard to distinguish the turbulence signal and small-scale noise, thus, difficult to isolate the effects of the SGS parameterization from other numerical and practical issues. Further analysis is necessary to clarify the effects of the SGS parameterization in the nested gray-zone simulations.

4. Summary and conclusions

This study investigated the effects of grid-size dependency in parameterized vertical heat transport to convective boundary layer (CBL) simulations at gray-zone resolutions. Our research was motivated by a few previous studies, which showed that conventional nonlocal PBL parameterizations, popularly used in mesoscale modeling, tends to excessively suppress resolved energy by parameterizing the total transport regardless of model resolution. Since there is no SGS transport parameterization designed for gray-zone simulations yet, we introduced a vertical transport algorithm for reducing the SGS heat transport by fitting to the LES output, based on the study of Shin and Hong (2013).

The algorithm possesses three features. First, nonlocal transport by the strong updrafts of organized structures and local transport by the remaining small-scale eddies are separately treated because they have different grid-size dependencies. Second, SGS nonlocal transport is calculated by multiplying a grid-size dependency function with the total nonlocal transport profile. The total nonlocal transport profile is obtained through linear fitting to the LES results, maintaining the basic role of nonlocal transport—cooling the surface layer, heating the mixed layer, and the entrainment. This is a complete change from the gradient-adjust gamma term in the K-profile models. Finally, SGS local transport is

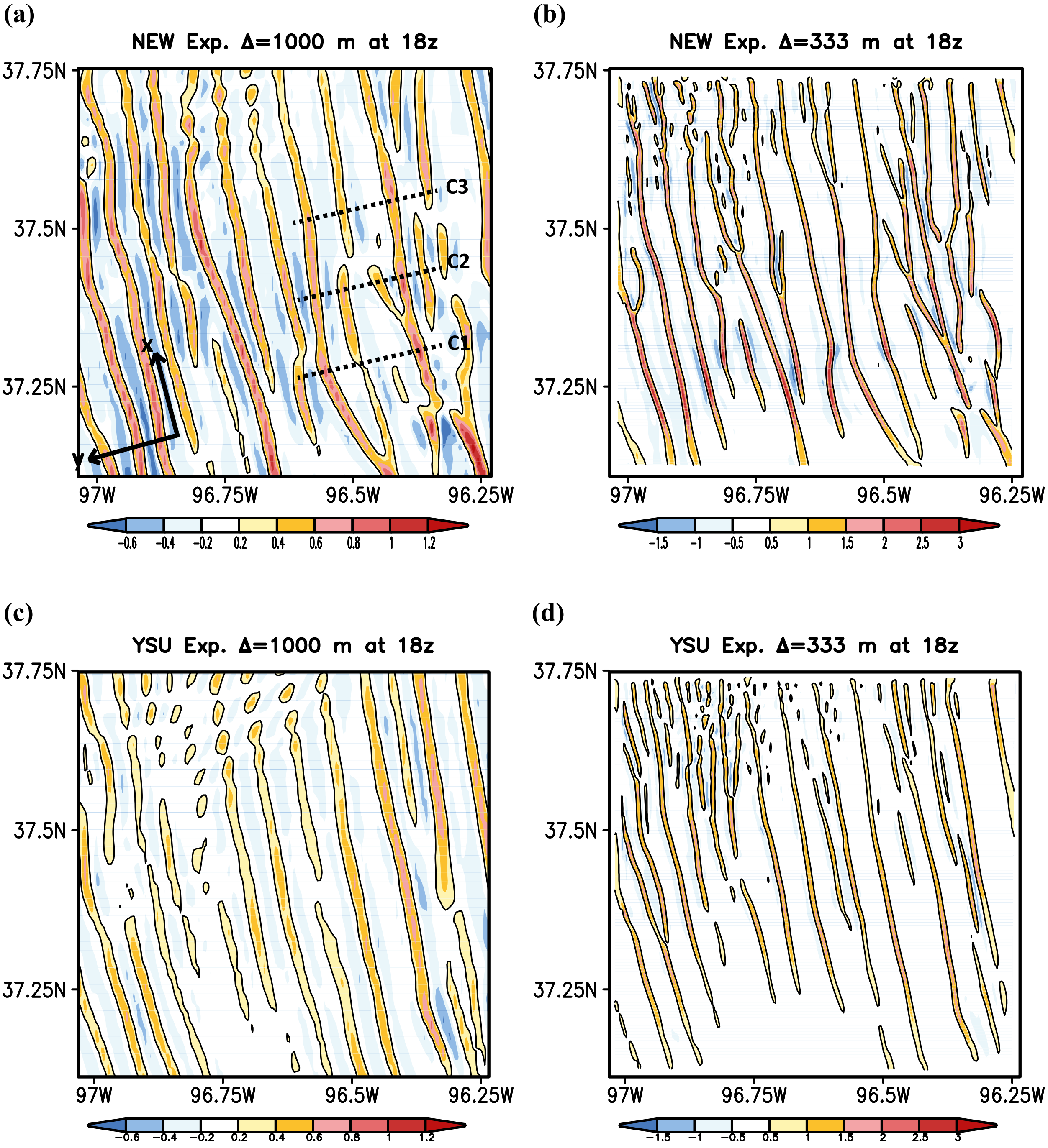

FIG. 13. Horizontal w distributions over the d04 area at 1800 UTC 20 Jun 2002 from (top) NEW and (bottom) YSU experiments for (a),(c) $\Delta = 1000$ m and (b),(d) $\Delta = 333$ m. Note that shaded intervals are different between the resolutions. Black contours are shown at $w = 0.2$ m s^{-1} for $\Delta = 1000$ m and 0.5 m s^{-1} for $\Delta = 333$ m. In (a), the roll coordinate and cross-roll lines (C1, C2, and C3) are shown (cf. section 3b).

formulated by multiplying a grid-size dependency with the total local transport profile. The total local transport is calculated using an eddy-diffusivity formula, as in the conventional PBL parameterization.

The results from the new algorithm were evaluated against the LES outcomes and compared with those from the conventional nonlocal, K-profile YSU PBL parameterization. Idealized CBLs forced by $(\overline{w'\theta'}_{\mathrm{SFC}}, U_g) = (0.20\,\mathrm{K\,m\,s^{-1}}, 10.0\,\mathrm{m\,s^{-1}})$ and $(0.05\,\mathrm{K\,m\,s^{-1}}, 10.0\,\mathrm{m\,s^{-1}})$ were simulated at gray-zone resolutions of $\Delta = 250$, 500, and 1000 m. The new algorithm produces mean temperature profiles closer to the LES results compared

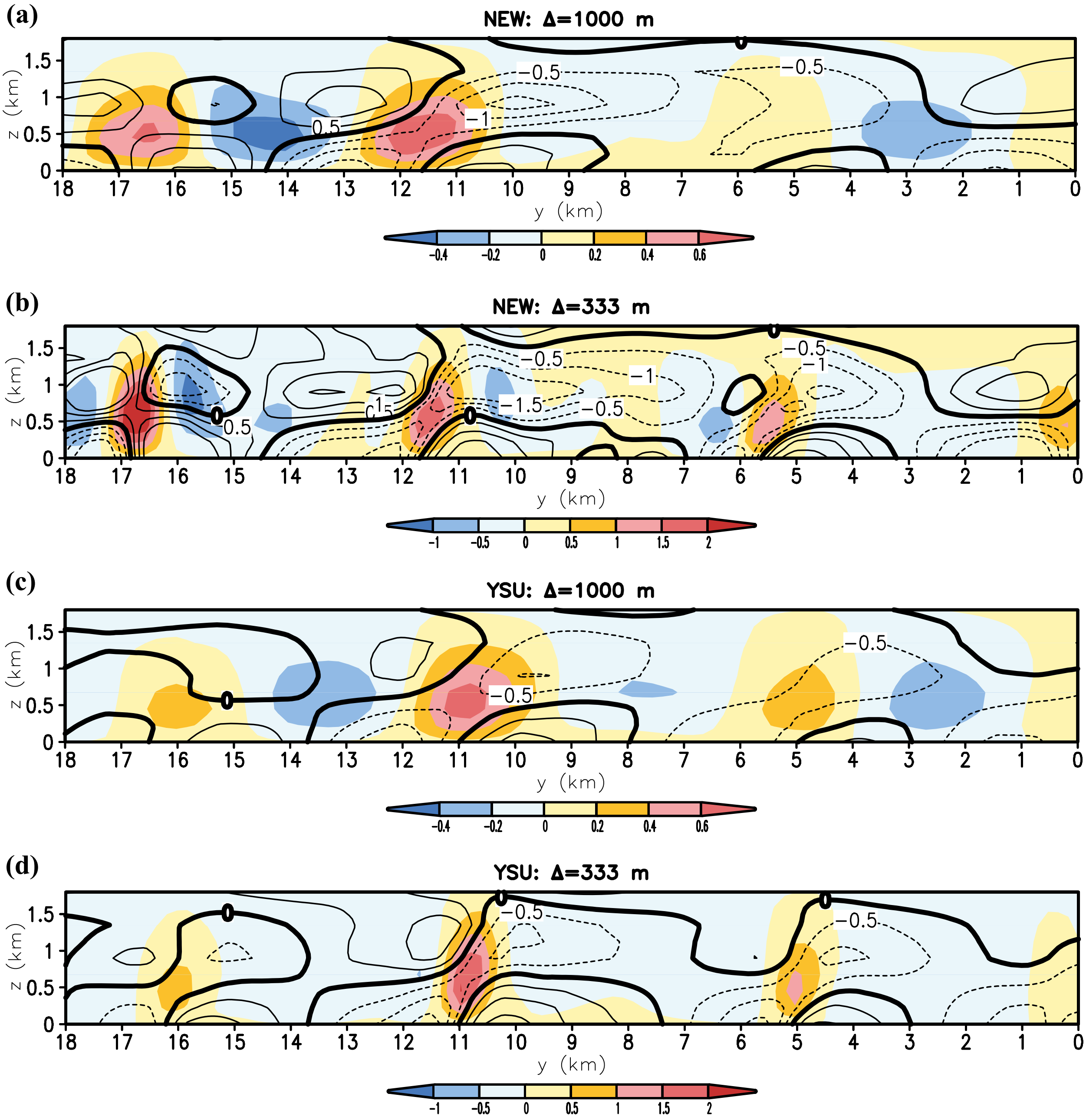

FIG. 14. The y–z cross sections of w (m s^{-1}) (shaded) and v_r (m s^{-1}) (contour) at 1800 UTC 20 Jun 2002 along the cross line C1 (cf. Fig. 13a): from the NEW experiment for (a) $\Delta = 1000$ m and (b) $\Delta = 333$ m, and from the YSU experiment for (c) $\Delta = 1000$ m and (d) $\Delta = 333$ m. Note that shaded intervals are different between the resolutions.

to the YSU scheme. Between the two biggest modifications from the YSU PBL scheme (a change in the total nonlocal transport profile and inclusion of the scale dependency), the improvement in the mean profiles is mainly due to the revised total nonlocal transport profile fit to the LES data. The grid-size dependency functions help the resolved motions and resolved transport profiles improved via accurately computing the SGS transport profiles at different resolutions. The time-averaged energy spectrum indicates the increase in resolved variability achieved by the SGS improvement. However, the new algorithm shows a spinup problem, and the quasi-equilibrium state is reached later than in the large-eddy simulation, consistent with a previous study by Ching et al. (2014). Application of the algorithm to the convective-roll simulations forced by the

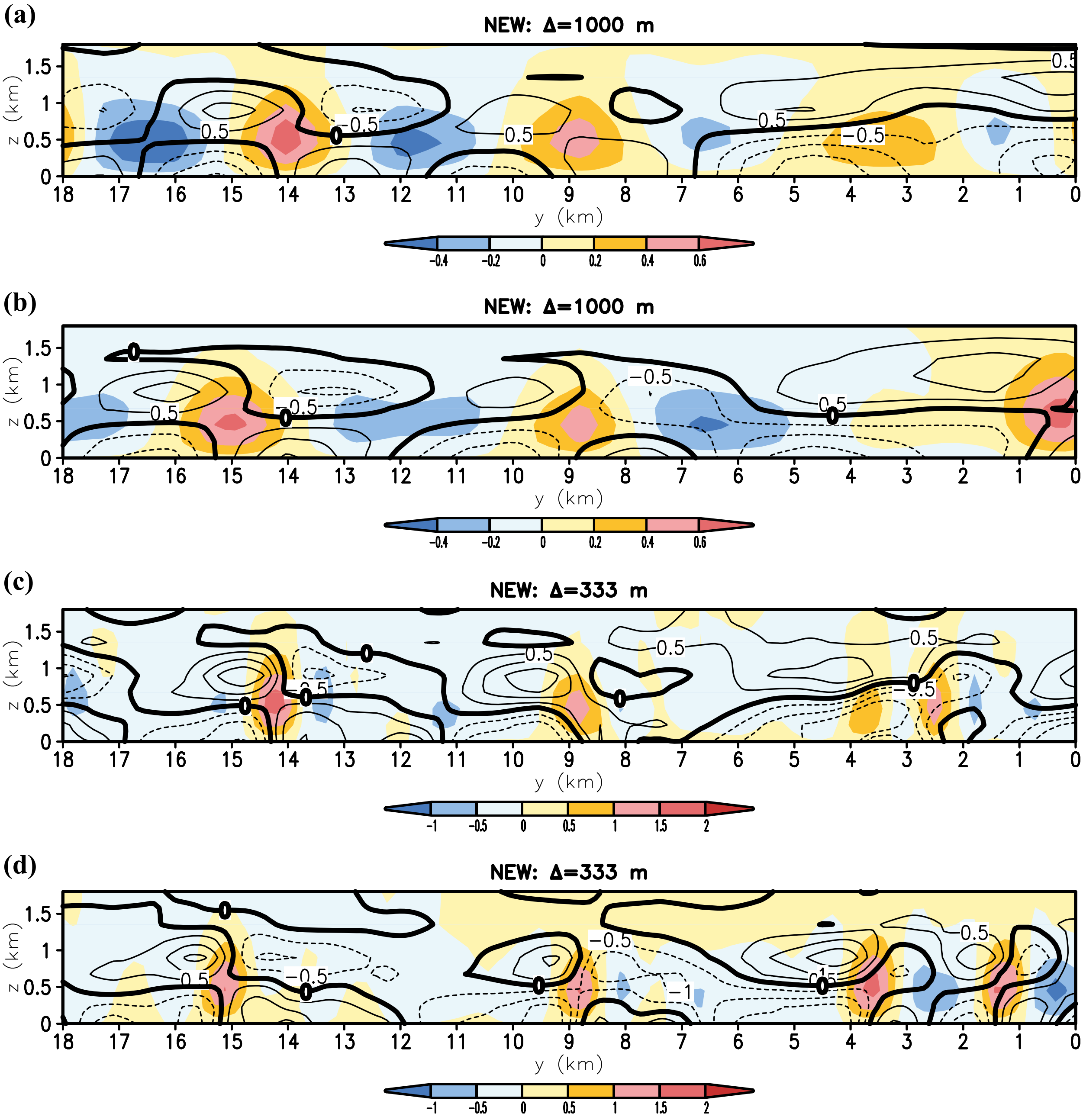

FIG. 15. The y–z cross sections of w (m s^{-1}) (shaded) and v_r (m s^{-1}) (contour) at 1800 UTC 20 Jun 2002 from the NEW experiment: for $\Delta = 1000$ m along the cross line (a) C2 and (b) C3 (cf. Fig. 13a), and for $\Delta = 333$ m along (c) C2 and (d) C3. Note that shaded intervals are different between the resolutions.

analysis data confirmed that the roll structures simulated by the new algorithm are more robust and the modeled circulations are stronger than the rolls produced by the conventional *K*-profile PBL parameterization.

Even though the new algorithm improved the gray-zone simulations in a three-dimensional simulation framework, the algorithm with the empirical fitting curve introduced here needs to be further improved and evaluated to cover more situations that occur in nature. The effects of surface and entrainment-layer wind shear, as well as the surface fluxes, are considered in the current prescribed profile, but the model is still limited to dry CBLs and does not cover moist convection situations (e.g., cloudy boundary layers). The parameterization for SGS momentum transport and scalar transports, and the spinup problem need to be further examined. For real-case simulations, there are several issues in high-resolution modeling, including numerics (e.g., discretization method, numerical filter), nesting methods, boundary conditions, and SGS parameterizations. These should be addressed in future work.

Acknowledgments. We gratefully acknowledge Jimy Dudhia and Peggy LeMone at NCAR whose thorough reviews improved the manuscript, Sungsu Park at NCAR for his comments and discussions on the work, and Yign Noh at YSU for his comments during the early stages of our study. We are also grateful to Sang-Hun Park at NCAR for his help in the use of the sixth-order filter in calculating the reference energy spectrum. The comments by the three anonymous reviewers improved the paper. This work has been partly carried out through the R&D project on the development of global numerical weather prediction systems of the Korea Institute of Atmospheric Prediction Systems (KIAPS) funded by the Korea Meteorological Administration (KMA). We would like to acknowledge high-performance computing support from Yellowstone (ark:/85065/d7wd3xhc) provided by NCAR's Computational and Information Systems Laboratory (CISL), sponsored by the National Science Foundation (NSF). The first author also thanks the Advanced Study Program (ASP) in NCAR for postdoctoral support.

APPENDIX

A Brief Summary of the Benchmark LES and Reference Data

The reference data were produced to quantify the resolved and SGS vertical transports for $25 \le \Delta \le 8000$ m. The benchmark LES was conducted for four CBL cases, which was driven by a constant surface heat flux ($\overline{w'\theta'_{\mathrm{SFC}}}$) and geostrophic wind in the x direction (U_g): ($\overline{w'\theta'_{\mathrm{SFC}}}$, U_g) = (0.20 K m s^{-1}, 5.0 m s^{-1}), (0.20 K m s^{-1}, 10.0 m s^{-1}), (0.05 K m s^{-1}, 10.0 m s^{-1}), and (0.05 K m s^{-1}, 15.0 m s^{-1}). Then, through spatially filtering the benchmark LES results for each Δ, the reference data were constructed.

a. The benchmark LES

For the benchmark LES run, the LES version of the WRF Model was used, and the simulation was performed over an 8 km × 8 km domain (D = 8 km) with a horizontal LES grid size of $\Delta_{\mathrm{LES}} = 25$ m. The model top is at 2 km with 100 vertical layers. Periodic boundary conditions were used in the x and y directions. For the LES SGS turbulence model, a three-dimensional parameterization using a TKE equation (Deardorff 1980) was used, with some modifications to consider the effects of grid anisotropies (Catalano and Moeng 2010; Scotti et al. 1993). Note that, in Shin and Hong (2013, hereafter SH13), the model top and the number of vertical layers used were 3.5 km and 120, respectively; they used Rayleigh damping in the upper 1 km. However, the differences in the benchmark LES setup do not change the findings in this study.

b. The reference data for the SGS transport

The benchmark LES domain ($D \times D$) consists of K grids (or subdomains) of size $\Delta \times \Delta$: $K = (D/\Delta)^2$. On the other hand, J LES grids of size $\Delta_{\mathrm{LES}} \times \Delta_{\mathrm{LES}}$ compose each subdomain $\Delta \times \Delta$: $J = (\Delta/\Delta_{\mathrm{LES}})^2$. Hereafter, the small letter k is used to refer to the kth subdomain in the LES domain, and j refers to the jth LES grid in the kth subdomain.

For each kth subdomain, the SGS vertical transport of any arbitrary variable ϕ is defined as

$$\overline{w'\phi'}^{\Delta_k} = J^{-1}\sum_j [(w_{j,k} - \overline{w}^{\Delta_k})(\phi_{j,k} - \overline{\phi}^{\Delta_k}) + F_{j,k}^{\mathrm{w}\phi}]. \quad \text{(A1)}$$

Here, $\overline{\phi}^{\Delta_k} = J^{-1}\sum_j \phi_{j,k}$ and $F_{j,k}^{\mathrm{w}\phi}$ is the SGS vertical transport at Δ_{LES} computed by the LES SGS model.

The SGS transport is decomposed into nonlocal and local transports (Siebesma and Cuijpers 1995; Siebesma et al. 2007). Here, the nonlocal transport is defined as the vertical transport via strong updrafts of coherent structures (e.g., thermals, rolls, and cells), and local transport via remaining small-scale turbulences:

$$\overline{w'\phi'}^{\Delta_k,\mathrm{NL}} \equiv a^{\Delta_k}(1 - a^{\Delta_k})(w_u^{\Delta_k} - w_e^{\Delta_k})(\phi_u^{\Delta_k} - \phi_e^{\Delta_k}), \quad \text{(A2)}$$

$$\overline{w'\phi'}^{\Delta_k,L} \equiv [a^{\Delta_k}\overline{w'\phi'}^{\Delta_k,u} + (1 - a^{\Delta_k})\overline{w'\phi'}^{\Delta_k,e}] + \overline{F^{w\phi}}^{\Delta_k}. \quad \text{(A3)}$$

The subscript u (e) denotes an average over the strong-updrafts (remaining environment) area for the kth subdomain. An overbar with the superscript u (e) refers to the average of fluctuations with respect to the strong-updrafts (remaining environment) averaged values. The a is the fractional area covered by the coherent structures.

It is worth noting that there is no unique and strict way to separate the nonlocal transport from the local transport. Identifying the coherent structures is a fundamental problem as there is no spectral gap between these two types of motion, and each conditional sampling method involves its own parameters that have no unique optimal values (Couvreux et al. 2010; Hellsten and Zilitinkevich 2013).

However, despite of the uncertainty in the sampling method there are several common features of the organized structures, regardless of the method used: the area fraction of the convective structures (less than 0.5) and the relative contribution of the nonlocal transport to the total (nonlocal plus local) transport (more than 50%) (LeMone 1976; Young 1988; Couvreux et al. 2010). SH13 showed that the two conditional sampling methods used for obtaining their grid-size dependency functions well reproduce the common characteristics (cf. section 4a and Fig. 8 in SH13). Moreover, the two methods came to the similar conclusion in terms of the two important parameters considered in the present study: the ratio of the SGS nonlocal transport (f_{nl}) to the total (nonlocal plus local) SGS transport, and the grid-size dependency functions of the nonlocal and local transports (P_{NL} and P_L).

For more details, refer to SH13. Note that SH13 produced their reference data based on previous studies by Dorrestijn et al. (2013) and Honnert et al. (2011).

REFERENCES

Angevine, W. M., 2005: How should entrainment be parameterized? *Workshop on the Parameterization of the Atmospheric Boundary Layer,* Los Angeles, CA, UCLA. [Available online at http://www.atmos.washington.edu/~breth/GCSS/Arrowhead200506/poster_ Angevine.pdf.]

Arakawa, A., J.-H. Jung, and C.-M. Wu, 2011: Toward unification of the multiscale modeling of the atmosphere. *Atmos. Chem. Phys.,* **11,** 3731–3742, doi:10.5194/acp-11-3731-2011.

Baldauf, M., A. Seifert, J. Forstner, D. Majewski, and M. Raschendorfer, 2011: Operational convective-scale numerical weather prediction with COSMO model: Description and sensitivities. *Mon. Wea. Rev.,* **139,** 3887–3905, doi:10.1175/MWR-D-10-05013.1.

Boutle, I. A., J. E. J. Eyre, and A. P. Lock, 2014: Seamless stratocumulus simulation across the turbulent gray zone. *Mon. Wea. Rev.,* **142,** 1655–1668, doi:10.1175/MWR-D-13-00229.1.

Brooks, I. M., and A. M. Fowler, 2012: An evaluation of boundary-layer depth, inversion and entrainment parameters by large-eddy simulation. *Bound.-Layer Meteor.,* **142,** 245–263, doi:10.1007/s10546-011-9668-3.

Brown, A. R., and A. L. M. Grant, 1997: Non-local mixing of momentum in the convective boundary layer. *Bound.-Layer Meteor.,* **84,** 1–22, doi:10.1023/A:1000388830859.

Bryan, G. H., and H. Morrison, 2012: Sensitivity of simulated squall line to horizontal resolution and parameterization of microphysics. *Mon. Wea. Rev.,* **140,** 202–225, doi:10.1175/MWR-D-11-00046.1.

——, J. C. Wyngaard, and J. M. Fritsch, 2003: Resolution requirements for the simulation of deep moist convection. *Mon. Wea. Rev.,* **131,** 2394–2416, doi:10.1175/1520-0493(2003)131<2394:RRFTSO>2.0.CO;2.

Catalano, F., and C.-H. Moeng, 2010: Large-eddy simulation of the daytime boundary layer in an idealized valley using the Weather Research and Forecasting numerical model. *Bound.-Layer Meteor.,* **137,** 49–75, doi:10.1007/s10546-010-9518-8.

Charles, M. E., and B. A. Colle, 2009: Verification of extratropical cyclones within the NCEP operational models. Part I: Analysis errors and short-term NAM and GFS forecasts. *Wea. Forecasting,* **24,** 1173–1190, doi:10.1175/2009WAF2222169.1.

Cheng, A., K.-M. Xu, and B. Stevens, 2010: Effects of resolution on the simulation of boundary-layer clouds and the partition of kinetic energy to subgrid scales. *J. Adv. Model. Earth Syst.,* **2** (1), doi:10.3894/JAMES.2010.2.3.

Ching, J., R. Rotunno, M. A. LeMone, A. Martilli, B. Kosovic, P. A. Jimenez, and J. Dudhia, 2014: Convectively induced secondary circulations in fine-grid mesoscale numerical weather prediction models. *Mon. Wea. Rev.,* **142,** 3284–3302, doi:10.1175/MWR-D-13-00318.1.

Clark, A. J., W. A. Gallus Jr., X. Xue, and F. Kong, 2009: A comparison of precipitation forecast skill between small convection-allowing and large convection-parameterizing ensembles. *Wea. Forecasting,* **24,** 1121–1140, doi:10.1175/2009WAF2222222.1.

Conzemius, R. J., and E. Fedorovich, 2006a: Dynamics of sheared convective boundary layer entrainment. Part I: Methodological background and large-eddy simulations. *J. Atmos. Sci.,* **63,** 1151–1178, doi:10.1175/JAS3691.1.

——, and ——, 2006b: Dynamics of sheared convective boundary layer entrainment. Part II: Evaluation of bulk model predictions of entrainment flux. *J. Atmos. Sci.,* **63,** 1179–1199, doi:10.1175/JAS3696.1.

Couvreux, F., F. Hourdin, and C. Rio, 2010: Resolved versus parametrized boundary-layer plumes. Part I: A parametrization-oriented conditional sampling in large-eddy simulations. *Bound.-Layer Meteor.,* **134,** 441–458, doi:10.1007/s10546-009-9456-5.

Davies, T., M. J. P. Cullen, A. J. Malcolm, M. H. Mawson, A. Staniforth, A. A. White, and N. Wood, 2005: A new dynamical core for the Met Office's global and regional modeling of the atmosphere. *Quart. J. Roy. Meteor. Soc.,* **131,** 1759–1782, doi:10.1256/qj.04.101.

Davis, C., and Coauthors, 2008: Prediction of landfalling hurricanes with the Advanced Hurricane WRF Model. *Mon. Wea. Rev.,* **136,** 1990–2005, doi:10.1175/2007MWR2085.1.

Deardorff, J. W., 1980: Stratocumulus-capped mixed layers derived from a three-dimensional model. *Bound.-Layer Meteor.,* **18,** 495–527, doi:10.1007/BF00119502.

——, G. E. Willis, and B. H. Stockton, 1980: Laboratory studies of the entrainment zone of a convective mixed layer. *J. Fluid Mech.,* **100,** 41–64, doi:10.1017/S0022112080001000.

Dorrestijn, J., D. T. Crommelin, A. P. Siebesma, and H. J. J. Jonker, 2013: Stochastic parameterization of shallow cumulus convection estimated from high-resolution model data. *Theor. Comput. Fluid Dyn.,* **27,** 133–148, doi:10.1007/s00162-012-0281-y.

Fiori, E., A. Parodi, and F. Siccardi, 2010: Turbulence closure parameterization and grid spacing effects in simulated supercell storms. *J. Atmos. Sci.,* **67,** 3870–3890, doi:10.1175/2010JAS3359.1.

Frech, M., and L. Mahrt, 1995: A two-scale mixing formulation for the atmospheric boundary layer. *Bound.-Layer Meteor.,* **73,** 91–104, doi:10.1007/BF00708931.

Hellsten, A., and S. Zilitinkevich, 2013: Role of convective structures and background turbulence in the dry convective boundary layer. *Bound.-Layer Meteor.,* **149,** 323–353, doi:10.1007/s10546-013-9854-6.

Holtslag, A. A. M., and B. A. Boville, 1993: Local versus nonlocal boundary-layer diffusion in a global climate model. *J. Climate,* **6,** 1825–1842, doi:10.1175/1520-0442(1993)006<1825:LVNBLD>2.0.CO;2.

Hong, S.-Y., and J. Dudhia, 2012: Next-generation numerical weather prediction: Bridging parameterization, explicit clouds, and large eddies. *Bull. Amer. Meteor. Soc.,* **93,** ES6–ES9, doi:10.1175/2011BAMS3224.1.

——, Y. Noh, and J. Dudhia, 2006: A new vertical diffusion package with an explicit treatment of entrainment processes. *Mon. Wea. Rev.,* **134,** 2318–2341, doi:10.1175/MWR3199.1.

Honnert, R., V. Masson, and F. Couvreux, 2011: A diagnostic for evaluating the representation of turbulence in atmospheric models at the kilometric scale. *J. Atmos. Sci.,* **68,** 3112–3131, doi:10.1175/JAS-D-11-061.1.

——, ——, and ——, 2014: What is new in the gray zone? *21st Symp. on Boundary Layers and Turbulence,* Leeds, United Kingdom, Amer. Meteor. Soc., 17B.2. [Available online at https://ams.confex.com/ams/21BLT/webprogram/Paper248579.html.]

Ito, J., H. Niino, M. Nakanishi, and C. H. Moeng, 2014: An extension of Mellor-Yamada type model to terra incognita scale. *21st Symp. on Boundary Layers and Turbulence,* Leeds, United Kingdom, Amer. Meteor. Soc., 66. [Available online at https://ams.confex.com/ams/21BLT/webprogram/Paper247833.html.]

Kaiser, R., and E. Fedorovich, 1998: Turbulence spectra and dissipation rates in a wind tunnel model of the atmospheric convective boundary layer. *J. Atmos. Sci.,* **55,** 580–594, doi:10.1175/1520-0469(1998)055<0580:TSADRI>2.0.CO;2.

Khairoutdinov, M. F., S. K. Krueger, C.-H. Moeng, P. A. Bogenschutz, and D. A. Randall, 2009: Large-eddy simulation of maritime deep tropical convection. *J. Adv. Model. Earth Syst.,* **1** (15), doi:10.3894/JAMES.2009.1.15.

Kim, S.-W., S.-U. Park, and C.-H. Moeng, 2003: Entrainment processes in atmospheric boundary layer structure driven by wind shear and surface heat flux. *Bound.-Layer Meteor.,* **108,** 221–245, doi:10.1023/A:1024170229293.

——, ——, D. Pino, and J. V.-G. de Arellano, 2006: Parameterization of entrainment in a sheared convective boundary layer using a first-order jump model. *Bound.-Layer Meteor.,* **120,** 455–475, doi:10.1007/s10546-006-9067-3.

Langhans, W., J. Schmidli, O. Fuhrer, S. Bieri, and C. Schar, 2013: Long-term simulations of thermally driven flows and orographic convection at convection-parameterizing and cloud-resolving resolutions. *J. Appl. Meteor. Climatol.,* **52,** 1490–1510, doi:10.1175/JAMC-D-12-0167.1.

LeMone, M. A., 1973: The structure and dynamics of horizontal roll vortices in the planetary boundary layer. *J. Atmos. Sci.,* **30,** 1077–1091, doi:10.1175/1520-0469(1973)030<1077:TSADOH>2.0.CO;2.

——, 1976: Modulation of turbulence energy by longitudinal rolls in an unstable planetary boundary layer. *J. Atmos. Sci.,* **33,** 1308–1320, doi:10.1175/1520-0469(1976)033<1308:MOTEBL>2.0.CO;2.

——, F. Chen, M. Tewari, J. Dudhia, B. Geerts, Q. Miao, R. L. Coulter, and R. L. Grossman, 2010: Simulating the IHOP_2002 fair-weather CBL with the WRF-ARW–Noah modeling system. Part II: Structures from a few kilometers to 100 km across. *Mon. Wea. Rev.,* **138,** 745–764, doi:10.1175/2009MWR3004.1.

——, M. Tewari, F. Chen, and J. Dudhia, 2013: Objectively determined fair-weather CBL depths in the ARW-WRF model and their comparison to CASES-97 observations. *Mon. Wea. Rev.,* **141,** 30–54, doi:10.1175/MWR-D-12-00106.1.

Lenschow, D. H., 1974: Model of the height variation of the turbulent kinetic energy budget in the unstable planetary boundary layer. *J. Atmos. Sci.,* **31,** 465–474, doi:10.1175/1520-0469(1974)031<0465:MOTHVO>2.0.CO;2.

Mahrt, L., and W. Gibson, 1992: Flux decomposition into coherent structures. *Bound.-Layer Meteor.,* **60,** 143–168, doi:10.1007/BF00122065.

Mirocha, J., B. Kosovic, and G. Kirkil, 2014: Resolved turbulence characteristics in large-eddy simulations nested within mesoscale simulations using the Weather Research and Forecasting Model. *Mon. Wea. Rev.,* **142,** 806–831, doi:10.1175/MWR-D-13-00064.1.

Moeng, C.-H., and P. P. Sullivan, 1994: A comparison of shear- and buoyancy-driven planetary boundary layer flows. *J. Atmos. Sci.,* **51,** 999–1022, doi:10.1175/1520-0469(1994)051<0999:ACOSAB>2.0.CO;2.

——, and A. Arakawa, 2012: Representation of boundary layer moisture transport in cloud-resolving models. *Mon. Wea. Rev.,* **140,** 3682–3698, doi:10.1175/MWR-D-12-00046.1.

——, P. P. Sullivan, M. F. Khairoutdinov, and D. A. Randall, 2010: A mixed scheme for subgrid-scale fluxes in cloud-resolving models. *J. Atmos. Sci.,* **67,** 3692–3705, doi:10.1175/2010JAS3565.1.

Noh, Y., W.-G. Cheon, S.-Y. Hong, and S. Raasch, 2003: Improvement of the K-profile model for the planetary boundary layer based on large eddy simulation data. *Bound.-Layer Meteor.,* **107,** 401–427, doi:10.1023/A:1022146015946.

Park, S.-H., J. B. Klemp, and W. C. Skamarock, 2014: A comparison of mesh refinement in the global MPAS-A and WRF Models using an idealized normal-mode baroclinic wave simulation. *Mon. Wea. Rev.,* **142,** 3614–3634, doi:10.1175/MWR-D-14-00004.1.

Pergaud, J., V. Masson, S. Malardel, and F. Couvreux, 2009: A parameterization of dry thermals and shallow cumuli for mesoscale numerical weather prediction. *Bound.-Layer Meteor.,* **132,** 83–106, doi:10.1007/s10546-009-9388-0.

Pleim, J. E., 2007: A combined local and nonlocal closure model for the atmospheric boundary layer. Part I: Model description and testing. *J. Appl. Meteor. Climatol.,* **46,** 1383–1395, doi:10.1175/JAM2539.1.

Saito, K., and Coauthors, 2006: The operational JMA nonhydrostatic mesoscale model. *Mon. Wea. Rev.,* **134,** 1266–1298, doi:10.1175/MWR3120.1.

Scotti, A., C. Meneveau, and D. K. Lilly, 1993: Generalized Smagorinsky model for anisotropic grids. *Phys. Fluids,* **5,** 2306, doi:10.1063/1.858537.

Seity, Y., P. Brousseau, S. Malardel, G. Hello, P. Benard, F. Bouttier, C. Lac, and V. Masson, 2011: The AROME-France convective-scale operational model. *Mon. Wea. Rev.,* **139,** 976–991, doi:10.1175/2010MWR3425.1.

Shin, H. H., and S.-Y. Hong, 2013: Analysis of resolved and parameterized vertical transports in convective boundary layers at gray-zone resolutions. *J. Atmos. Sci.,* **70,** 3248–3261, doi:10.1175/JAS-D-12-0290.1.

Siebesma, A. P., and J. W. M. Cuijpers, 1995: Evaluation of parametric assumptions for shallow cumulus convection. *J. Atmos. Sci.,* **52,** 650–666, doi:10.1175/1520-0469(1995)052<0650:EOPAFS>2.0.CO;2.

——, P. M. M. Soares, and J. Teixeira, 2007: A combined eddy-diffusivity mass-flux approach for the convective boundary layer. *J. Atmos. Sci.,* **64,** 1230–1248, doi:10.1175/JAS3888.1.

Skamarock, W. C., 2004: Evaluating mesoscale NWP models using kinetic energy spectra. *Mon. Wea. Rev.,* **132,** 3019–3032, doi:10.1175/MWR2830.1.

——, and Coauthors, 2008: A description of the Advanced Research WRF version 3. NCAR Tech. Note NCAR/TN-475+STR, 113 pp. [Available online at http://www.mmm.ucar.edu/wrf/users/docs/arw_v3_bw.pdf.]

Takemi, T., and R. Rotunno, 2003: The effects of subgrid model mixing and numerical filtering in simulations of mesoscale cloud systems. *Mon. Wea. Rev.,* **131,** 2085–2010, doi:10.1175/1520-0493(2003)131<2085:TEOSMM>2.0.CO;2.

Troen, I., and L. Mahrt, 1986: A simple model of the atmospheric boundary layer; sensitivity to surface evaporation. *Bound.-Layer Meteor.,* **37,** 129–148, doi:10.1007/BF00122760.

Weckwerth, T. M., and Coauthors, 2004: An overview of the International H_2O Project (IHOP_2002) and some preliminary highlights. *Bull. Amer. Meteor. Soc.,* **85,** 253–277, doi:10.1175/BAMS-85-2-253.

Weisman, M. L., J. B. Klemp, and R. Rotunno, 1988: Structure and evolution of numerically simulated squall lines. *J. Atmos. Sci.,* **45,** 1990–2013, doi:10.1175/1520-0469(1988)045<1990:SAEONS>2.0.CO;2.

——, C. Davis, W. Wang, K. W. Manning, and J. B. Klemp, 2008: Experiences with 0–36-h explicit convective forecasts with the WRF-ARW Model. *Wea. Forecasting,* **23,** 407–437, doi:10.1175/2007WAF2007005.1.

Wyngaard, J. C., 2004: Toward numerical modeling in the ''terra incognita.'' *J. Atmos. Sci.,* **61,** 1816–1826, doi:10.1175/1520-0469(2004)061<1816:TNMITT>2.0.CO;2.

Young, G. S., 1988: Turbulence structure of the convective boundary layer. Part II: Phoenix 78 aircraft observations of thermals and their environment. *J. Atmos. Sci.,* **45,** 727–735, doi:10.1175/1520-0469(1988)045<0727:TSOTCB>2.0.CO;2.